Geophys. J. Int. (2003) **155,** 1021–1041

Quantitative analysis of seismic fault zone waves in the rupture zone of the 1992 Landers, California, earthquake: evidence for a shallow trapping structure

Zhigang Peng,[1] Yehuda Ben-Zion,[1] Andrew J. Michael[2] and Lupei Zhu[3]

[1] *Department of Earth Sciences, University of Southern California, Los Angeles,* CA 90089-0740, *USA. E-mail: zpeng@email.usc.edu*
[2] *United States Geological Survey,* MS 977, 345 *Middlefield Rd, Menlo Park,* CA 94025, *USA*
[3] *Department of Earth and Atmospheric Sciences, Saint Louis University, St Louis,* MO 63103, *USA*

Accepted 2003 August 13. Received 2003 July 13; in original form 2003 March 06

SUMMARY

We analyse quantitatively a waveform data set of 238 earthquakes recorded by a dense seismic array across and along the rupture zone of the 1992 Landers earthquake. A grid-search method with station delay corrections is used to locate events that do not have catalogue locations. The quality of fault zone trapped waves generated by each event is determined from the ratios of seismic energy in time windows corresponding to trapped waves and direct *S* waves at stations close to and off the fault zone. Approximately 70 per cent of the events with *S*–*P* times of less than 2 s, including many clearly off the fault, produce considerable trapped wave energy. This distribution is in marked contrast with previous claims that trapped waves are generated only by sources close to or inside the Landers rupture zone. The time difference between the *S* arrival and trapped waves group does not grow systematically with increasing hypocentral distance and depth. The dispersion measured from the trapped waves is weak. These results imply that the seismic trapping structure at the Landers rupture zone is shallow and does not extend continuously along-strike by more than a few kilometres. Synthetic waveform modelling indicates that the fault zone waveguide has depth of approximately 2–4 km, a width of approximately 200 m, an *S*-wave velocity reduction relative to the host rock of approximately 30–40 per cent and an *S*-wave attenuation coefficient of approximately 20–30. The fault zone waveguide north of the array appears to be shallower and weaker than that south of the array. The waveform modelling also indicates that the seismic trapping structure below the array is centred approximately 100 m east of the surface break.

Key words: fault zones, inversion, trapped waves, waveform analysis.

1 INTRODUCTION

Major crustal faults are often marked by narrow tabular or wedge-shaped low-velocity zones. An accurate determination of the fault zone (FZ) properties at depth can improve the understanding of earthquake processes and parameters, long-term evolution of faults and more (e.g. Aki & Richards 2002; Scholz 2002; Sibson 2002; Ben-Zion & Sammis 2003). Measurements associated with inactive exhumed fault zones (e.g. Chester & Chester 1998; Evans *et al.* 2000; Faulkner *et al.* 2003) and surface ruptures of active faults (e.g. Sieh *et al.* 1993; Johnson *et al.* 1994, 1997) give direct information on FZ properties. However, these studies are limited to structures presently at the surface. Various indirect geophysical methods such as gravity, electromagnetic surveys, reflection/refraction seismology and traveltime tomography have been used to image FZ structures at depth (Mooney & Ginzburg 1986; Ben-Zion & Sammis 2003, and references therein). Recently, Fialko *et al.* (2002) inferred, from InSAR observations of surface deformation near the rupture zone of the 1999 Hector Mine earthquake, on the existence of belts of damaged FZ rock that are a few kilometres in width. In general, these techniques can only resolve blurred versions of the true subsurface FZ structures.

Waveform modelling of FZ trapped waves can provide high-resolution imaging of coherent low-velocity FZ layers at depth. FZ trapped waves follow the direct body wave arrivals and are large-amplitude, low-frequency, dispersive wave trains that are produced by constructive interference of critically reflected waves inside low-velocity FZ layers. Over the last decade, Li and co-workers argued, based on an analysis of small waveform data sets in several places, for the existence of $\approx$100 m wide FZ layers that extend to the bottom of the seismogenic zone (e.g. $>$10 km). Locations for which such claims were made include the Parkfield segment of the San Andreas fault (Li & Leary 1990), the Anza segment of the San Jacinto fault (Li & Vernon 2001), the rupture zones of the 1992 Landers

earthquake (Li *et al.* 1994a,b, 2000), the 1995 Kobe earthquake (Li *et al.* 1998) and the 1999 Hector Mine earthquake (Li *et al.* 2002). On the other hand, analyses of large data sets associated with the Karadere–Duzce branch of the North Anatolian fault (Ben-Zion *et al.* 2003) and the Parkfield segment of the San Andreas fault (Michael & Ben-Zion 1998; Korneev *et al.* 2003) indicate that the trapping structures in those locations are relatively shallow (e.g. ≈3 km) FZ layers that are largely above the depth sections with active seismicity.

Igel *et al.* (2002), Jahnke *et al.* (2002) and Fohrmann *et al.* (2003) showed with 3-D calculations that sources well outside and below shallow FZ layers can produce ample trapped waves energy at stations close to the FZ. In contrast, the generation of trapped waves in a low-velocity FZ layer that is continuous with depth requires sources that are inside or very close to the low-velocity structure. Thus, observations of FZ trapped waves due to sources well outside the fault imply that the trapping structure is shallow. Ben-Zion *et al.* (2003) referred to trapped waves (motion amplification and long-period oscillations) in FZ stations due to sources not necessarily in the fault as 'FZ-related site effects'.

In this paper we analyse a waveform data set (Lee 1999) produced by 238 aftershocks of the 1992 Landers earthquake and recorded by a dense seismic array across the Landers rupture zone. Seismograms generated by some events in our data set have been analysed previously by Li *et al.* (1994a,b), who concluded on the existence of a low-velocity FZ waveguide that extends continuously to the bottom of the seismogenic zone. In contrast, our analysis indicates that the seismic trapping structure at the Landers rupture zone extends only to a depth of approximately 2–4 km. Our conclusion is based on spatial distributions of events that produce FZ-related site effects, traveltime moveout of body *S* and trapped waves, dispersion analysis and synthetic waveform modelling of FZ waves. The waveform modelling indicates further that the shallow trapping structure has an effective width of approximately 200 m with a centre approximately 100 m east of the surface break below the array, an *S*-wave velocity decrease of approximately 30–40 per cent relative to the host rock and an *S*-wave attenuation coefficient of approximately 20–30. The waveguide north of the array is less pronounced (e.g. smaller velocity contrast, narrower FZ width) than that south of the array.

2 ANALYSIS

2.1 Experiment and event location

A dense seismic FZ array was deployed across and along the rupture zone of the 1992 Landers, California, $M_w = 7.3$ earthquake to observe FZ trapped waves (Li *et al.* 1994a,b; Lee 1999). The geometry of the array is shown in the inset of Fig. 1. It consisted of an east–west line along the Encantado road crossing the rupture zone northwest of Landers and two north–south lines. The east–west line included 22 three-component, short-period L-22 seismometers with instrument spacing 25 m within 200 m of the surface break and 50–100 m further away. In this work we analyse systematically a seismic waveform data set generated by 238 aftershocks in the period 1992 October 14–17, and recorded by the dense FZ array. A much larger data set was recorded by Li *et al.* (1994a) but has not been released in a form available for analysis. A subset of 93 earthquakes of our events was also recorded by the Caltech/USGS Southern California Seismic Network (SCSN). Fig. 1 shows the locations of these 93 earthquakes based on the Richards-Dinger & Shearer (2000) relocated catalogue.

We developed a grid-search method augmented by station corrections to locate the events that were recorded only by the FZ array. The grid-search method uses accurately picked *P* arrivals and *S–P* times and determines locations by minimizing the L2 norm of traveltime residuals between observed data and synthetic calculations. The latter are produced by a 1-D velocity model for the region near the Landers rupture zone (Hauksson *et al.* 1993). The source depth is also included in the grid search.

We first apply this method to locate a subset of 67 events that have catalogue locations and *S–P* times of less than 4.5 s (or hypocentral distances within approximately 35 km). Waveforms generated by earthquakes with a hypocentral distance larger than 35 km usually have low signal-to-noise ratios in seismograms recorded by the FZ array and are ignored. Fig. 2 shows the catalogue locations (solid circles) of these 67 events and locations produced by the grid-search method (red ellipses). The size of the ellipse marks the standard deviations of horizontal location errors. As seen in the figure, most events are relocated by the grid-search method further away from the FZ. This can be partially explained by the existence of a low-velocity FZ and the use of a laterally uniform 1-D velocity model in our method. For example, first arrivals at stations east of the array from events west of the FZ will be later than expected in a laterally homogenous model. Our grid-search method thus tends to put such events further to the west (away from the FZ) to satisfy their arrival times.

To reduce the effects of lateral velocity variation on our location determinations, we apply corrections based on the residuals between the observed and synthetic traveltimes. As shown in the inset of Fig. 2, the traveltime residuals for events with backazimuth (BAZ) between 0° and 172° (east) and BAZ between 172° and 360° (west) of the FZ are quite different. We calculate two sets of station delays by averaging the traveltime residuals for events west and east of the FZ, and apply these station delays to the synthetic calculations to relocate the events. The locations after incorporating the station delay corrections are shown as blue ellipses in Fig. 2. The average horizontal and vertical differences between the obtained locations and the corresponding catalogue locations of the 67 events are 3.0 and 3.6 km, respectively. These values provide estimates of the location errors produced by our grid-search method together with station delay corrections, which we apply to obtain hypocentral parameters for the events that do not have catalogue locations.

2.2 Spatial distribution of events generating trapped waves

The spatial distribution of earthquakes producing FZ trapped waves at surface FZ stations provides first-order information on overall properties of the trapping structure. Previous studies used visual inspection to identify FZ trapped waves and to determine the quality of their generation. Although straightforward, visual inspection is subjective and not efficient when dealing with a large data set having thousands of waveforms. Here we determine the quality of FZ trapped waves generation from the ratios of trapped waves energy to *S*-wave energy at stations relatively close to and stations off the FZ.

The procedure employed is as follows: the energy in a seismogram recorded at each station within a specified time window is approximated by summing the squares of velocity amplitudes and normalizing by the length of the time window (Fohrmann *et al.* 2003). The *S*-wave window starts 0.1 s before the *S* arrival and ends at the start of the trapped waves window. The boundary between the

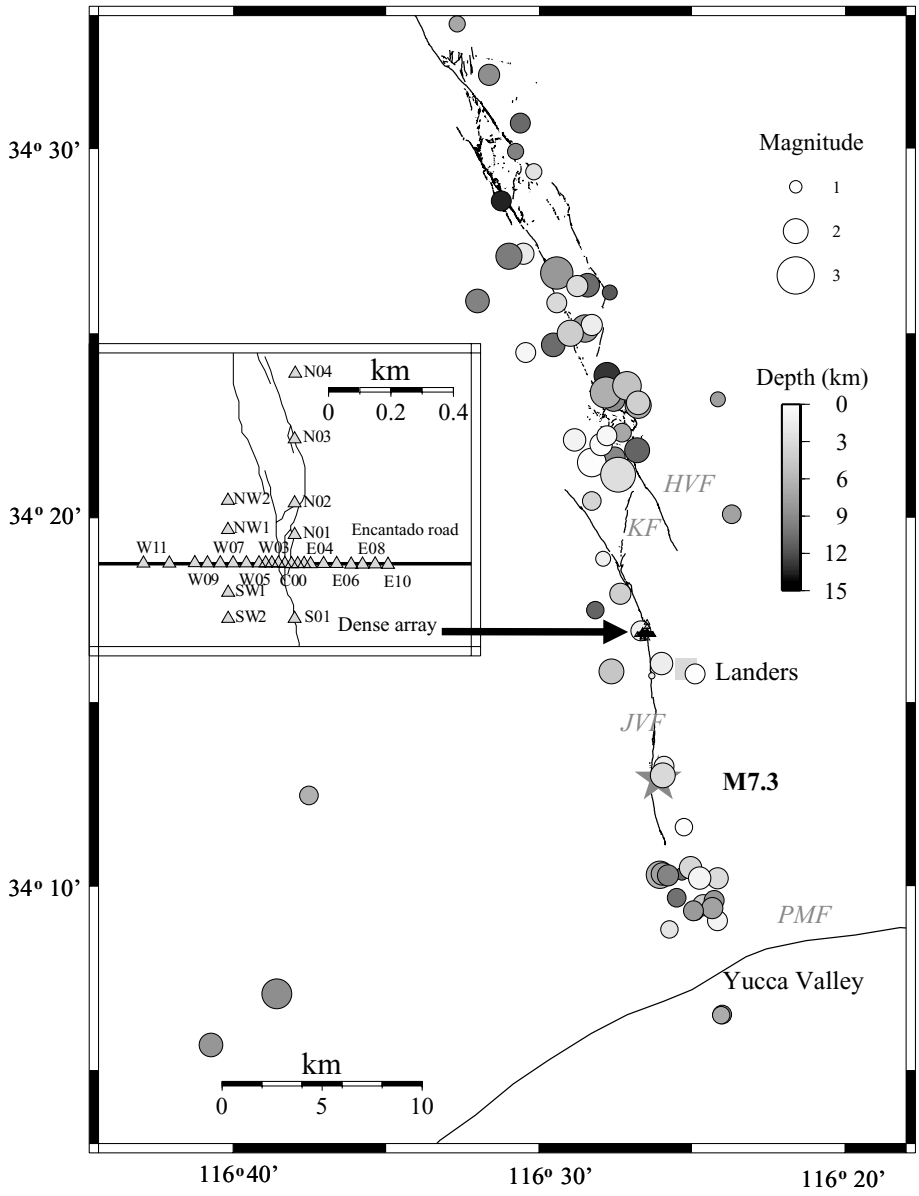

Figure 1. Epicentres of 93 aftershocks (circles) of the 1992 Landers, California, earthquake (star) recorded by the SCSN. The event magnitudes are in the range 0.5 and 3.1 and event depths range from 0 to 14 km. The lines indicate surface traces of the Johnson Valley fault (JVF), Kickapoo fault (KF), Homestead Valley fault (HVF), and Pinto Mountain fault (PMF). The inset shows the geometry of the dense seismic array around the Landers rupture zone.

windows is determined by maximizing the resulting energy ratio using a shear body waveform length in the range 0.3–0.7 s. Such a range excludes the trapped waves in our data set (if they exist) and ensures that at least two cycles are included in the *S*-wave window. The end of the trapped waves window is the time when the amplitude reduces back to that of the *S* wave. Examples of the employed time windows are shown in Figs 4–6 below. We then divide the energy calculated for FZ trapped waves by that of the direct *S* wave to obtain the energy ratio for each seismogram. The average energy ratios for seismograms recorded at 13 stations (W02–E06, S01–N03) with clear trapped waves and within 400 m of the FZ, and 13 stations (W11–W03, E07–E10) relatively far from the FZ are computed and named AR_{FZ} and AR_{OFF}, respectively. Finally, our measure for the quality of trapped waves generation is the ratio AR_{FZ}/AR_{OFF}. We note that the 13 selected FZ stations are not symmetric with respect to the surface trace of the Landers rupture (or station C00) because of the observed asymmetry of stations that record clear trapped waves. This is reflected in the contour maps of the normalized amplitude spectra distribution versus station positions as illustrated in Figs 4(b) and 5(b) below, and the synthetic waveform modelling described in Section 2.5. Waveforms recorded at station SW2, SW1, NW1 and NW2 are not used in the calculation since these four stations were not in operation during the first 2 days of the experiment.

Figs 3(a) and (b) show the locations, coded with quality of FZ trapped waves generation, of 198 events located by our grid search and station corrections and a subset of 60 events that have catalogue locations, respectively. The energy ratios against the *S–P* times for the 198 events are given in the inset of Fig. 3(a). Energy ratios are not calculated for events with clipped waveforms and *S–P* times of more than 4.5 s. Energy ratios exceeding 4, between 2 and 4, and less than 2 are assigned, respectively, quality A, B and C of trapped waves

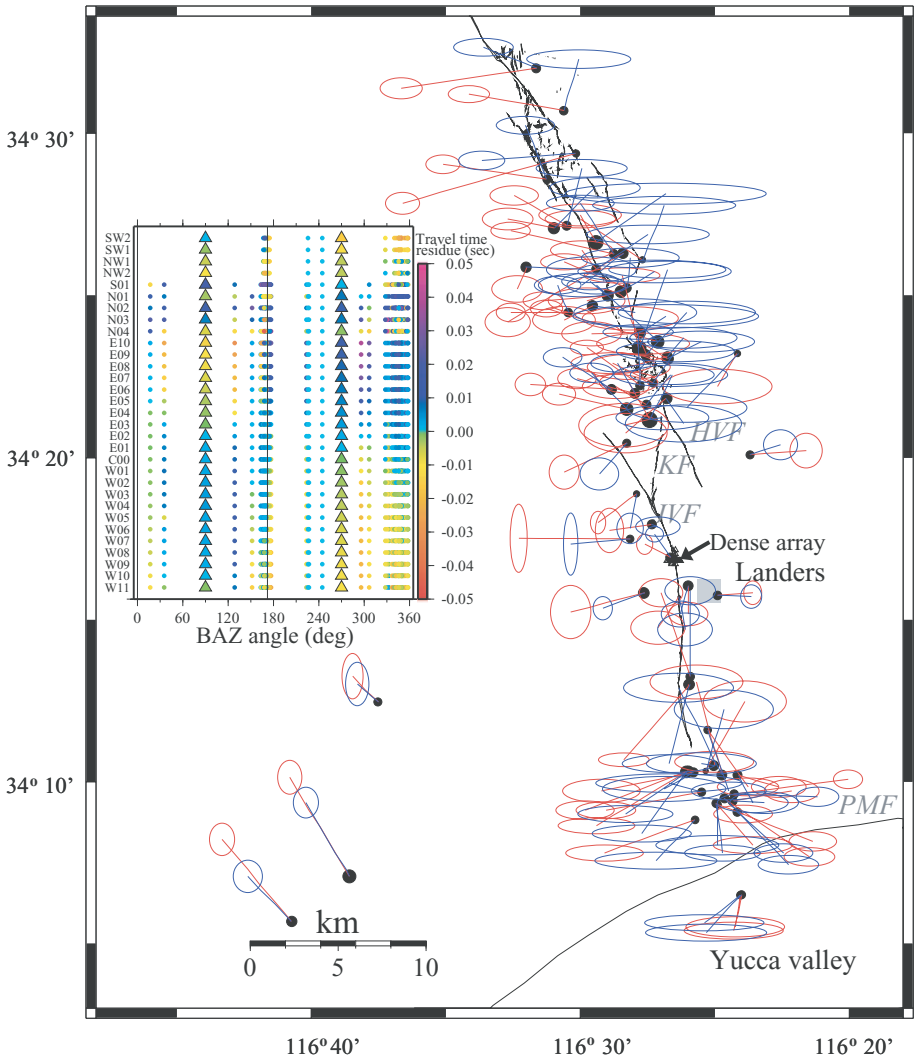

Figure 2. (a) Comparison of catalogue locations (solid circles) of 67 events and locations produced by the grid-search method before (red ellipses) and after (blue ellipses) station delay corrections. Other symbols and notations are same as in Fig. 1. The inset shows traveltime residuals versus backazimuth (BAZ) for the 67 events. The small dots are colour-coded by the value of the residuals with red being negative and blue being positive. The two vertical lines with BAZ values of 0 and 172° mark the boundaries of regions east and west of the FZ. The big triangles denote the averaged residuals for events east and west of the FZ.

generation. These choices suggest themselves from the distribution of the calculated ratios and are marked in Fig. 3 with stars, triangles and circles, respectively. Using slightly different values of energy ratios will not affect our overall conclusion on the spatial distribution of events generating trapped waves.

Several important observations can be made from the spatial distribution of earthquakes producing trapped waves. Approximately 70 per cent of nearby events with an *S–P* time of less than 2 s, including many clearly off the fault, generate FZ trapped waves with quality A or B. This distribution is in marked contrast with previous claims that trapped waves are generated only by sources close to or inside the Landers rupture zone (e.g. Li *et al.* 1994a,b, 2000). Furthermore, we find that approximately 30 per cent of the events north of the intersection of the Johnson Valley fault with the Kickapoo fault also generate trapped waves with quality A or B at the FZ array. This suggests that the branching at the Kickapoo fault does not have a dominant effect on the generation of trapped waves by events north of it. As mentioned before, the existence of trapped waves due to sources outside the Landers rupture zone indicates that the trapping structure is shallow. The percentage of events generating FZ trapped waves with energy ratios greater than 2 (quality A or B) is compatible with that estimated by Fohrmann *et al.* (2003) using 3-D finite-difference calculations.

Figs 4–6 give representative fault-parallel seismograms associated with each quality category of FZ trapped waves. As shown in Figs 4 and 5, waveforms recorded at the 13 stations close to the fault trace (marked with large bold fonts) have large-amplitude oscillations with relatively low frequency after the *S* arrivals. In contrast, such waveform characteristics are much weaker or absent at the 13 stations located further away from the FZ. Fig. 4(b) gives a contour map of normalized amplitude spectra versus positions of 22 stations across the FZ for event 10161332 with a quality A trapped waves generation. The clear concentration of 4–6 Hz energy at stations W01–E05 is associated with the FZ trapped waves recorded (Fig. 4a) at stations close to the FZ. For events with a quality B trapped waves generation, there is still considerable low-frequency energy at stations close to the FZ (Fig. 5b). However, the spectral energy is more scattered compared with that of Fig. 4(b). For events with quality

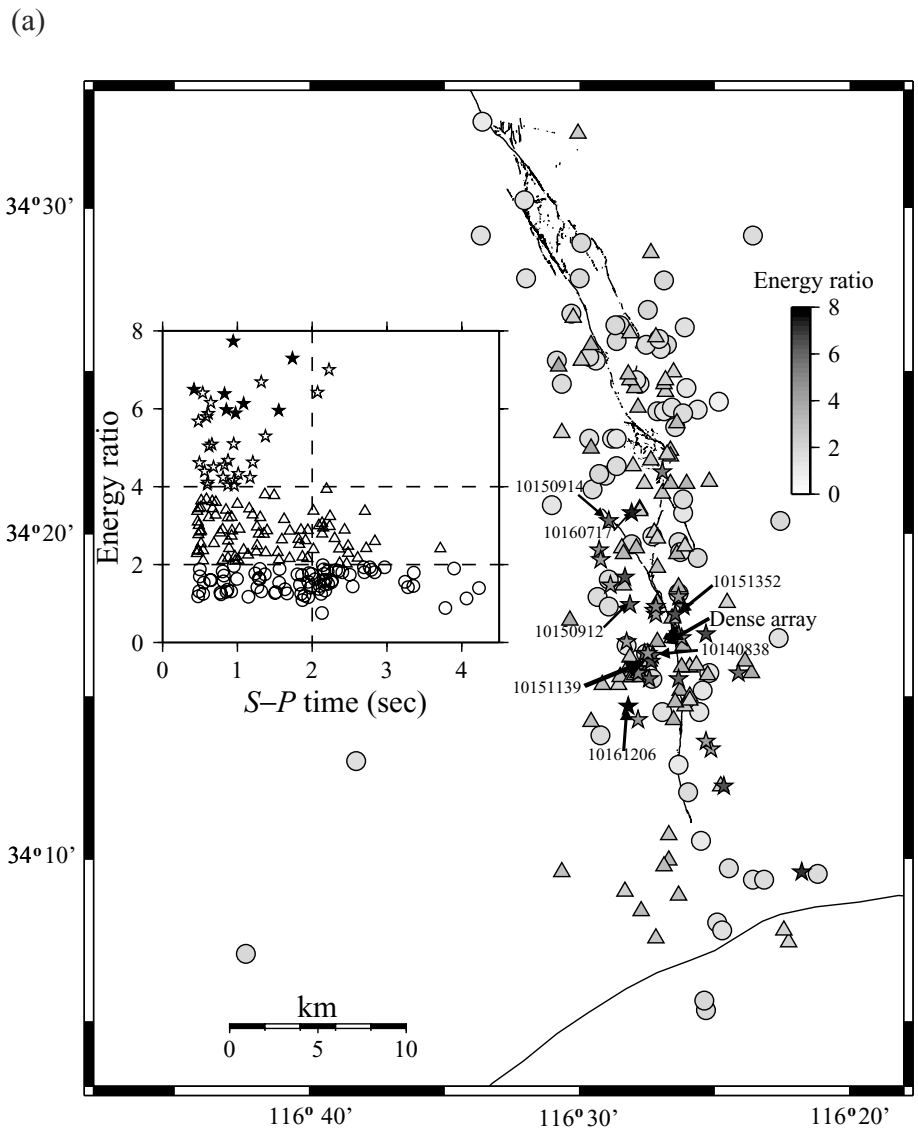

Figure 3. (a) Quality of trapped waves generation for 198 events located using the grid-search method and station delay corrections based on ratios of trapped waves energy divided by *S*-wave energy (inset). Energy ratios larger than 4, between 2 and 4, and less than 2, are denoted by stars, triangles, and circles, respectively. Approximately 70 per cent of the events with *S–P* times less than 2 s (vertical line in the inset) generate FZ trapped waves with an energy ratio exceeding 2. There are 34 events with quality A trapped waves generation and 86 events with quality B. Dispersion curves measured from waveforms of the eight events (stars) pointed by arrows are shown in Fig. 12(b). The waveforms of these events are modelled in Figs 13 and 14. The event ID numbers consist of two-digit month, two-digit day, two-digit hour and two-digit minute. (b) Quality of trapped waves generation for 60 events that have catalogue locations. There are four events with quality A trapped waves generation and 26 events with quality B. The events pointed by arrows are used in later analysis.

C trapped waves generation, the discussed trapped waves features recorded at the dense array are diffused and scattered in both the time histories (Fig. 6a) and amplitude spectra (Fig. 6b).

2.3 Traveltime moveout analysis

To place bounds on the depth extent of the structure generating FZ trapped waves at the Landers rupture zone, we examine the time delay between the direct *S* wave and the trapped waves. The time difference, or moveout, between the *S* phase and trapped waves should increase with propagation distance in the low-velocity trapping structure. This is illustrated in Fig. 7 with synthetic seismograms generated using the 2-D analytical solution of Ben-Zion & Aki (1990) and Ben-Zion (1998) for antiplane *S* waves in a half-space (HS) containing a low-velocity FZ layer (Fig. 8). The *S*-wave velocity and attenuation coefficient of the HS are $\beta_{\rm HS} = 3$ km s^{-1} and $Q_{\rm HS} = 1000$. The corresponding material properties and width of the FZ layer are $\beta_{\rm FZ} = 2$ km s^{-1}, $Q_{\rm FZ} = 50$ and $W = 200$ m. The source is an *SH* line dislocation with a unit step function in time and is located at position x_S, z_S. The synthetic calculations of Fig. 7 are performed for a source at the interface between the FZ and the left-hand block and a receiver on the free surface at the centre of the FZ layer.

Fig. 9(a) shows fault-parallel seismograms at FZ station E02 generated by 32 earthquakes with *S–P* times of less than 2 s that are assigned quality A for FZ trapped waves generation. The data are

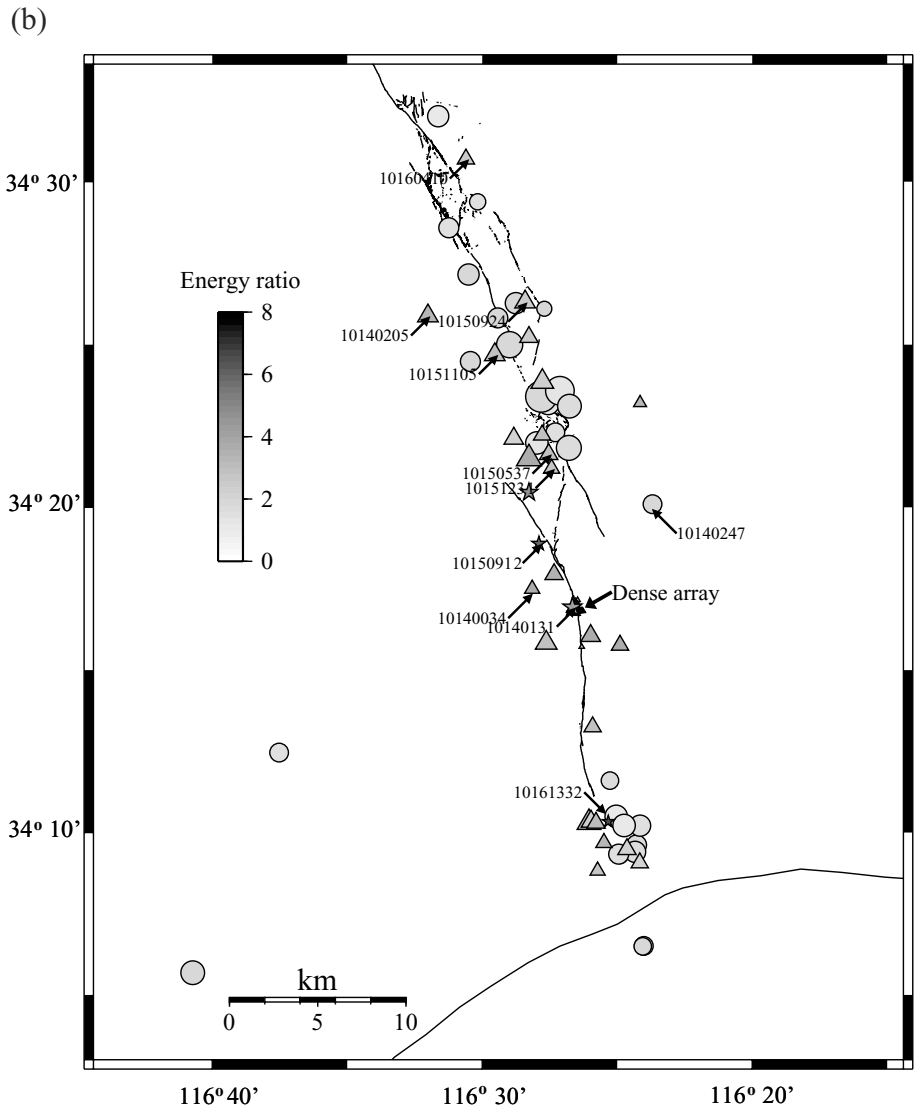

Figure 3. (*Continued.*)

separated into two groups based on their locations north or south of the array. The time differences between the *S* arrivals and centres of trapped waves group for these seismograms are plotted in Fig. 9(b) against hypocentral distances. Clearly, there is no persistent moveout between the *S* wave and the trapped waves group as the hypocentral distances increase. This implies that the propagation distance inside the low-velocity FZ layer is approximately the same for all the events. The average time delay for the events south of the array is larger than that for events north of the array, suggesting different waveguide properties for the FZ south and north of the array.

As discussed in Ben-Zion *et al.* (2003), the propagation distances of the trapped waves inside the low-velocity FZ material can be estimated from

$$z_S = \frac{2\beta_{\rm HS}\beta_{\rm FZ}}{\beta_{\rm HS} - \beta_{\rm FZ}}\Delta t, \qquad (1)$$

where Δt is the time between the direct *S* arrival and the centre of the trapped waves group. If the hypocentres of the events generating FZ trapped waves are deep enough for the wavefield to sample the entire depth extent of the waveguide, Eq. (1) can be used to estimate the depth of the waveguide. This was done by Ben-Zion *et al.* (2003) using cross-sections of events in the depth range 5–15 km around the Karadere–Duzce branch of the North Anatolian fault. In our case, some of the events used in Figs 9(a) and (b) have catalogue depths that are shallower than 3 km, and most do not have catalogue locations.

To estimate the depth extent of the waveguide using eq. (1), we measure the time delay between the direct *S* wave and trapped waves for events with quality A or B that have catalogue locations and hypocentres deeper than 6 km. Fig. 9(c) shows fault-parallel seismograms at FZ station E02 generated by seven earthquakes located at different epicentral distances north of the array. The event locations are marked in Fig. 3(b). The time delays between the direct *S* arrival and the centre of the trapped waves group do not grow with increasing hypocentral distances. The average time delay is 0.39 s, similar to the 0.34 s value obtained from the 14 events in Fig. 9(b) north of the array with quality A trapped waves generation. As discussed in Section 2.5, synthetic waveform modelling of FZ waves generated by four events north of the array indicates that the average (or effective) *S*-wave velocities of the HS and FZ material are approximately 3.2 and 2.3 km s^{-1}, respectively. Using these values together with $\Delta t = 0.39$ s in eq. (1) gives z_S of approximately

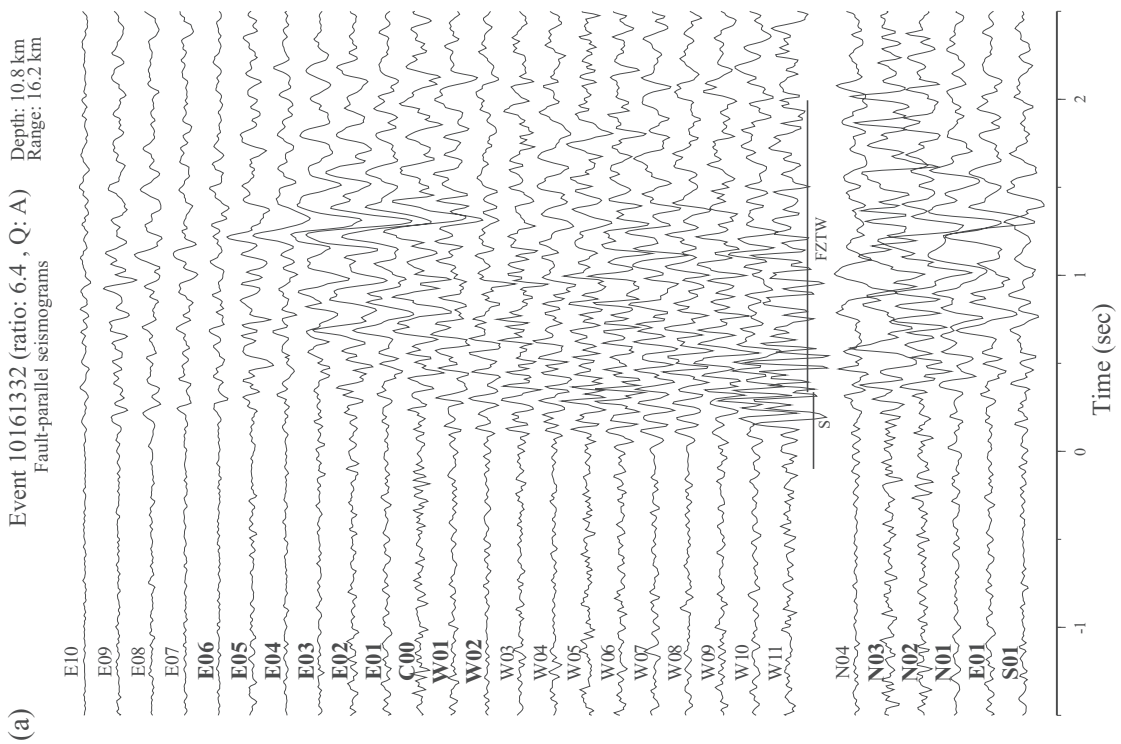

Figure 4. (a) Fault-parallel seismograms recorded at the dense array stations for event 10161332. The two short horizontal lines mark time windows for the *S* wave and FZ trapped waves used in the energy ratio calculations. Station names are marked on the traces with stations close to the FZ given in a large bold font. The focal depth and range (hypocentral distance) of the event are marked in the top right-hand corner. The event location is shown in Fig. 3(b) and is assigned quality A trapped waves generation. (b) Normalized amplitude spectra versus position of stations across the FZ for event 10161332.

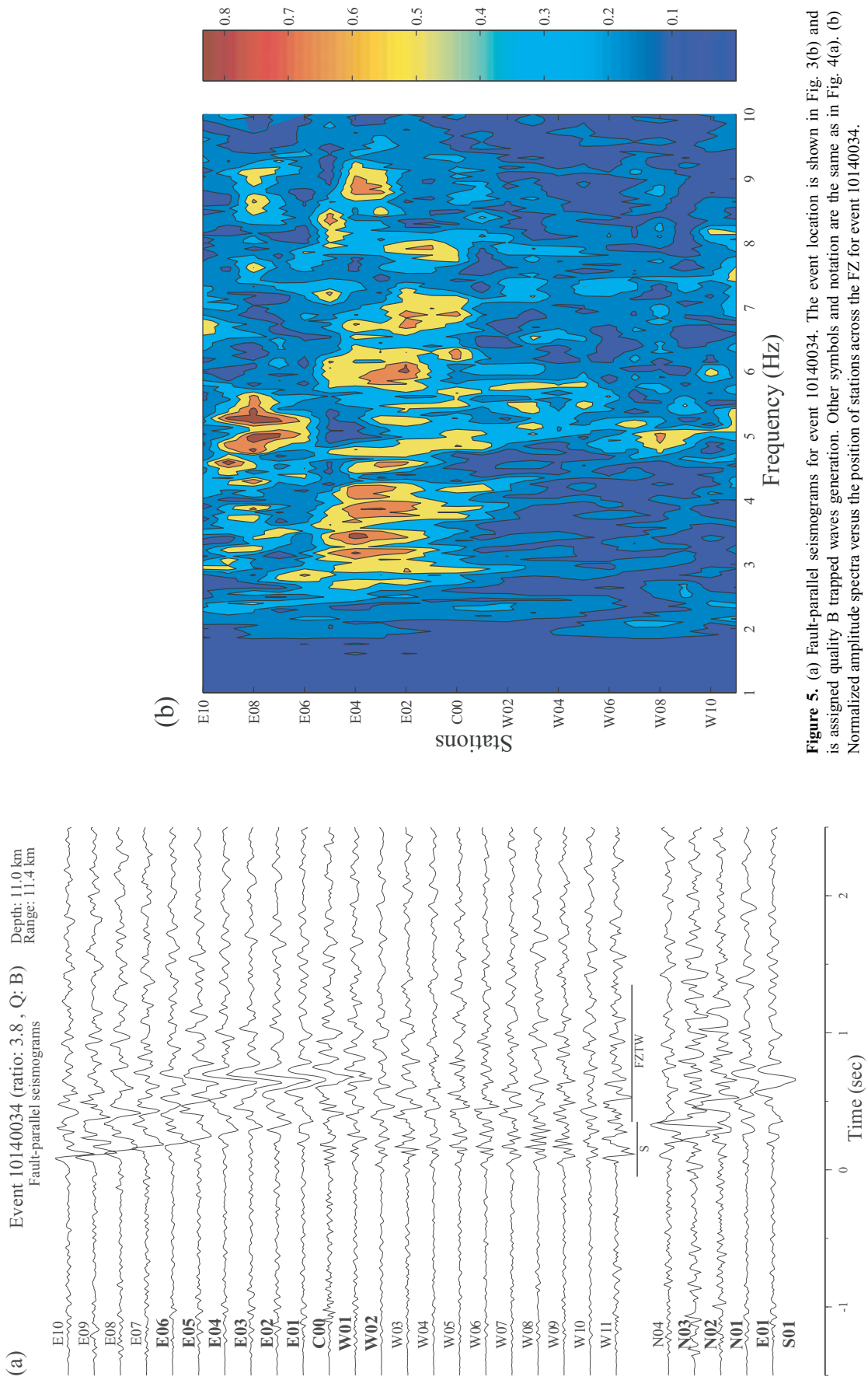

Figure 5. (a) Fault-parallel seismograms for event 10140034. The event location is shown in Fig. 3(b) and is assigned quality B trapped waves generation. Other symbols and notation are the same as in Fig. 4(a). (b) Normalized amplitude spectra versus the position of stations across the FZ for event 10140034.

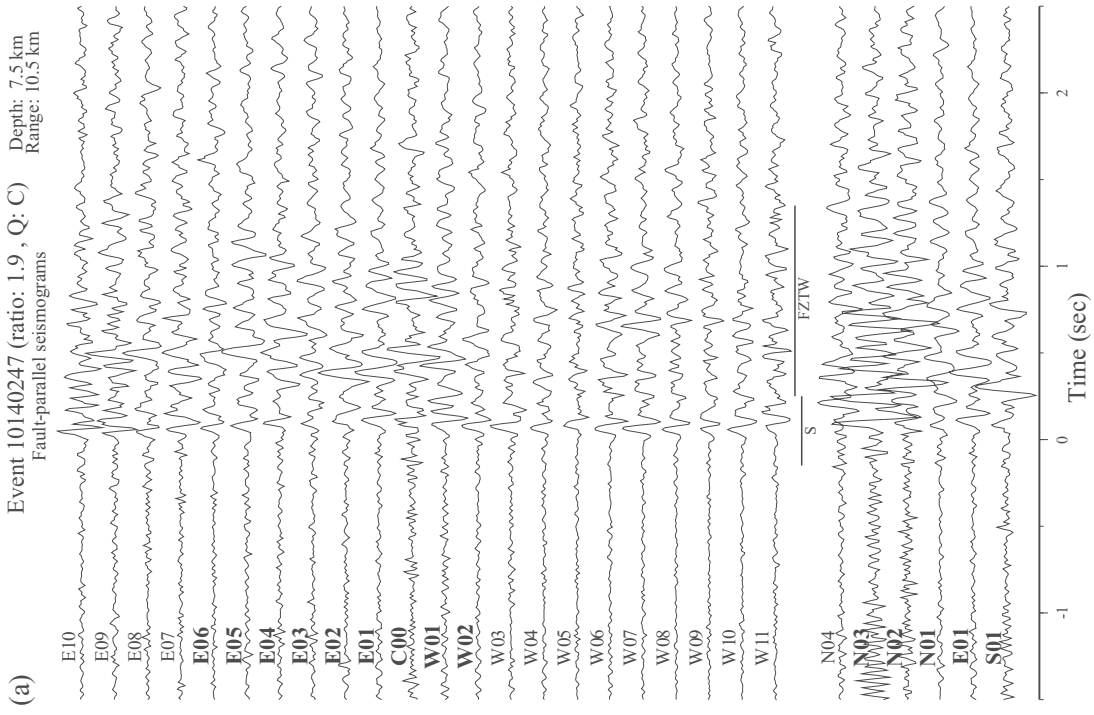

Figure 6. (a) Fault-parallel seismograms for event 10140247. The event location is shown in Fig. 3(b) and is assigned quality C trapped waves generation. Other symbols and notation are the same as in Fig. 4(a). (b) Normalized amplitude spectra versus the position of stations across the FZ for event 10140247.

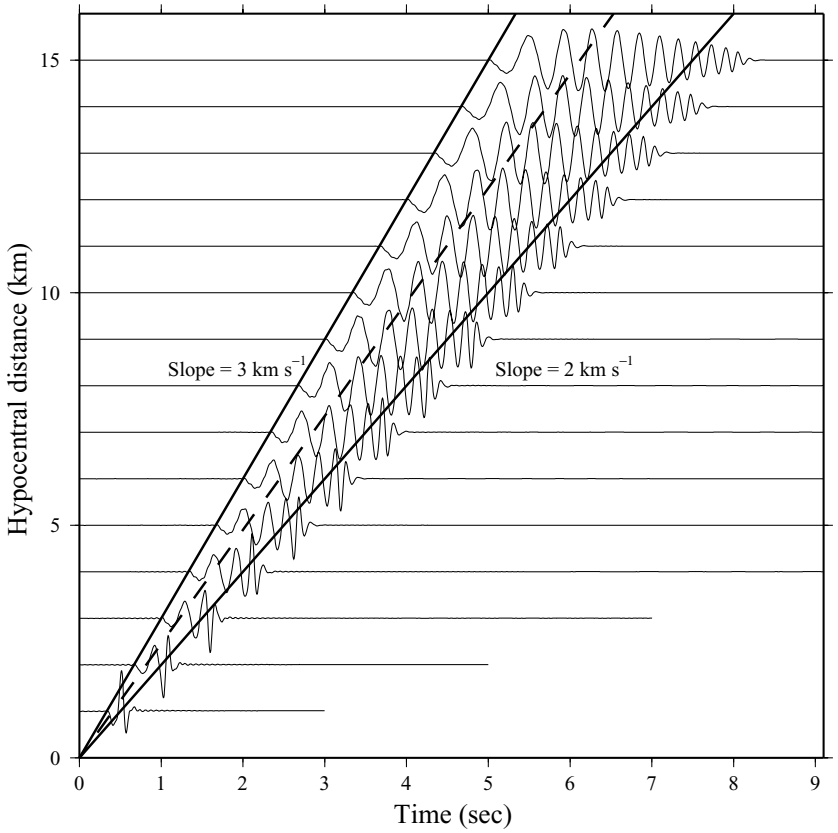

Figure 7. Synthetic seismograms generated by the 2-D analytical solution of Ben-Zion & Aki (1990) and Ben-Zion (1998) for different propagation distances along the FZ. The two solid lines with slopes β_{HS} and β_{FZ} mark, respectively, the arrival time of the *S* phase and the end of the trapped waves group (defined as the time when the amplitude returns to that of the *S* arrival). The dashed line marks the centre of the trapped waves group. Group velocities measured from the synthetic seismograms are shown in Fig. 11(b).

6.4 km. This value is smaller than the hypocentral depths of most events. Moreover, since the seven events are located at considerable epicentral distances from the array, the actual propagation paths of the FZ trapped waves must include along-strike components. If we assume for simplicity that the average along-strike component and vertical component are the same, we obtain an estimated waveguide depth of approximately 4.5 km. The waveform modelling discussed in Section 2.5 suggests an upper bound of approximately 3 km for the FZ waveguide north of the array.

In the region south of the array, only four out of nine events with catalogue depth larger than 6 km produce trapped waves with quality A or B. Also, the traveltime data for the events south of the array have a large scatter with a possible bi-modal distribution (Fig. 9b). We therefore do not use the traveltime data to estimate the depth of the FZ waveguide south of the array. However, the waveform modelling of Section 2.5 suggests an upper bound for the FZ waveguide in that region of approximately 4 km. The results of this section imply that the trapping structure at the Landers rupture zone consist of a relatively shallow low-velocity waveguide that is discontinuous along strike. The results are compatible with the spatial distribution of events generating trapped waves discussed in Section 2.2, and the dispersion analysis discussed next.

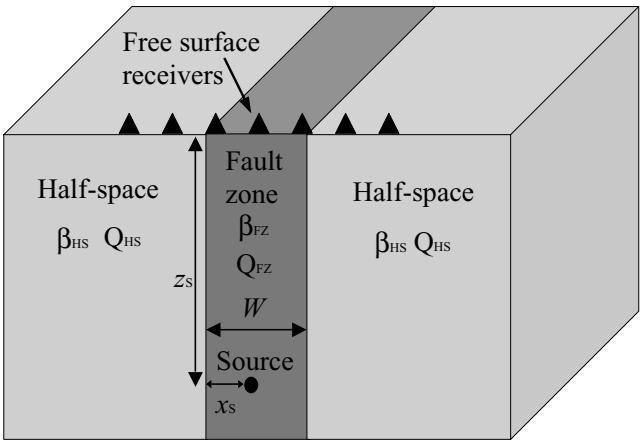

Figure 8. A three-media model for a uniform low-velocity FZ structure in a half-space. The source is an SH line dislocation with coordinates (x_S, z_S). The width, shear attenuation coefficient and shear wave velocity of the FZ are marked by W, Q_{FZ}, and β_{FZ}. The shear wave velocity and the attenuation coefficient of the HS are denoted by β_{HS} and Q_{HS}.

2.4 Dispersion analysis

To study the dispersion of FZ trapped waves, we measure group velocities from multiple bandpass-filtered seismograms using a zero-phase Gaussian filter. Before analysing the observed data, we describe the method and discuss trade-offs in model parameters using synthetic calculations. Fig. 10(a) shows filtered synthetic seismograms in 17 frequency bands of 0.5 Hz over the range 2–10 Hz. The material properties and FZ width used to generate the seismograms are $\beta_{HS} = 3$ km s^{-1}, $Q_{HS} = 1000$, $\beta_{FZ} = 2$ km s^{-1}, $Q_{FZ} = 1000$ and $W = 200$ m. Here and in the following sections we fix the

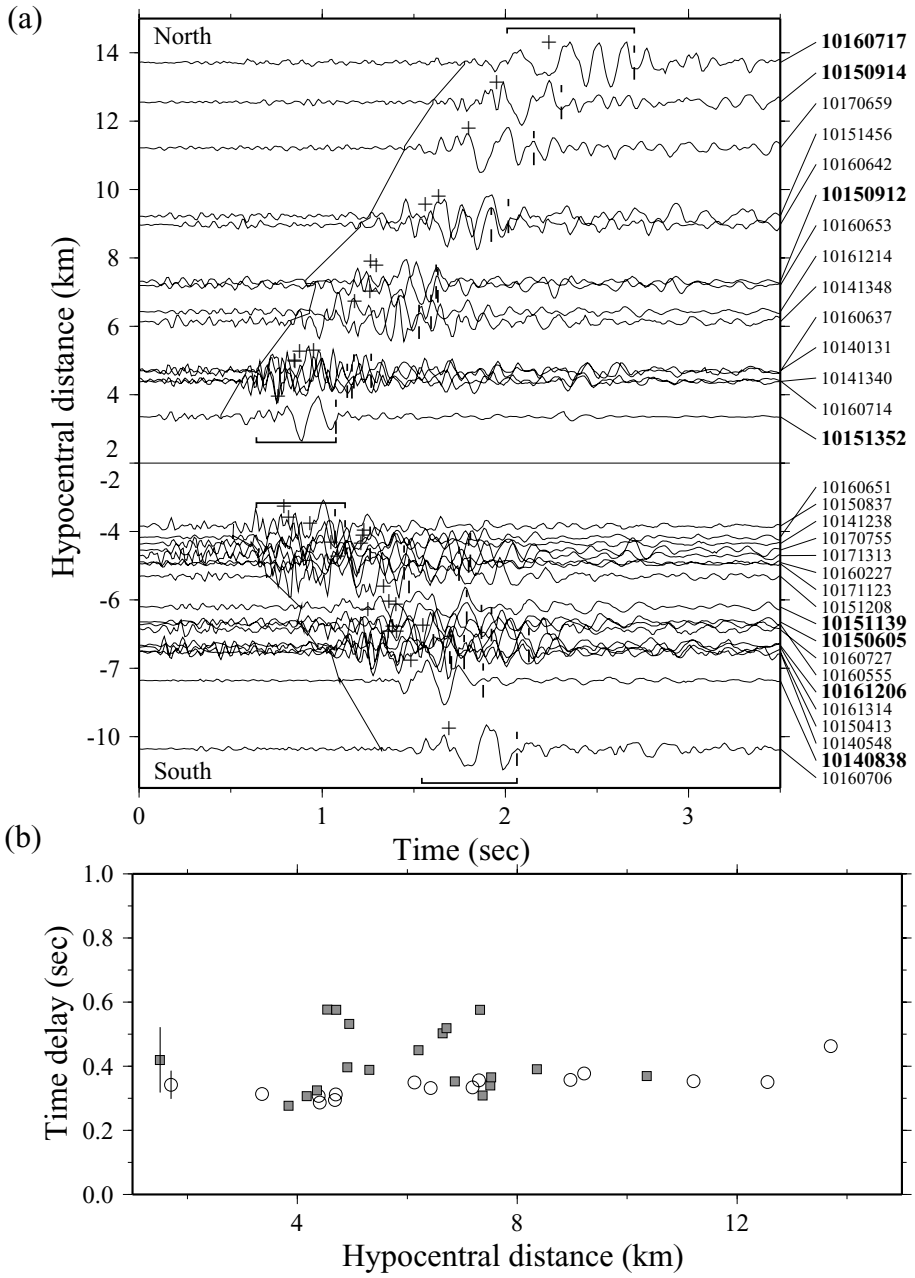

Figure 9. (a) Fault-parallel seismograms at station E02 for 32 events with quality A trapped waves generation. The waveforms are plotted against their hypocentral distances and aligned with *P* arrivals at time 0. The thin diagonal lines mark the *S* arrival time for each seismogram. The horizontal bars below and above the seismograms denote the approximate start and end of FZ trapped waves groups. The plus sign on top of each seismogram marks the centre of the trapped waves group. The vertical dashed line marks the end of the trapped waves group, measured as the mid-position between the *S* arrival and the time when the amplitude reduces back to that of the *S* wave. The ID numbers of the earthquakes are given on the right (see the explanation in the caption of Fig. 3). Waveforms of the eight events for which the ID numbers are given in large bold font are modelled in Figs 13 and 14. Dispersion curves measured from the waveforms of these eight events are shown in Fig. 12(b). (b) Time differences between the *S* arrival and centres of the trapped waves group versus hypocentral distances for the 32 events. Squares and circles denote the values for events south and north of the array, respectively. The symbols on the left with vertical lines give the mean and standard deviations of the time differences. The lack of systematic increase with hypocentral distance implies an approximately constant propagation length in the FZ waveguide. (c) Fault-parallel seismograms at FZ station E02 generated by seven earthquakes north of the array with hypocentral depth larger than 6 km. The seismograms are aligned with *S* arrivals at time 0. The two vertical dashed lines mark the time of the *P* arrival and the end of the trapped waves group. The plus sign on top of each seismogram denotes the estimated centre of the FZ trapped waves group. The time delay between the direct *S* arrival and the centre of the trapped waves group are indicated above each trace. The ID numbers of the earthquakes are given on the left. The range (hypocentral distances) and focal depth of each event are marked in the top right-hand side of each seismogram. The event locations are shown in Fig. 3(b).

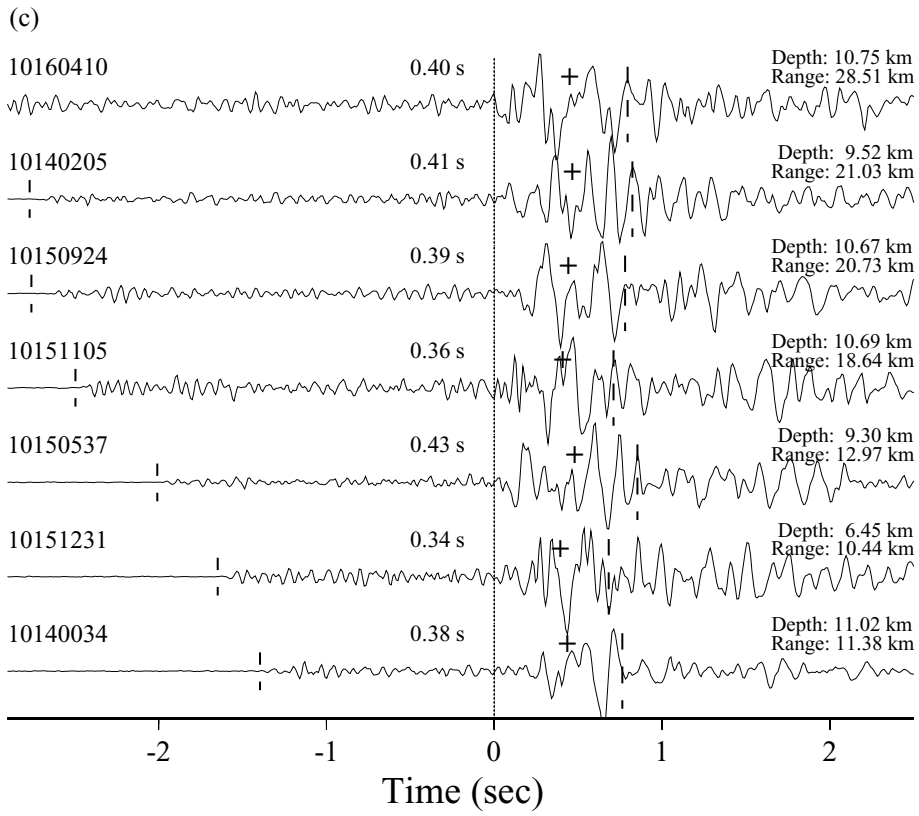

Figure 9. (*Continued.*)

attenuation factor of the HS to be 1000. The propagation distance in the FZ layer is 5 km. The circles in the right-hand panel mark the peaks of the envelopes calculated by Hilbert transforms of the bandpass-filtered seismograms. Each peak provides a measure for the arrival of energy at the specified frequency band. As expected, the trapped waves at lower frequencies travel faster than those at higher frequencies.

Fig. 10(b) provides a comparison between analytical and measured dispersion curves. The stars are group velocities measured from the filtered synthetic seismograms in Fig. 10(a). The lines are generated by the analytical dispersion formula of Ben-Zion & Aki (1990) for a vertical FZ layer in an HS,

$$\tan\left[W 2\pi f \left(\beta_{\rm FZ}^{-2} - c^{-2}\right)^{1/2}\right] = \frac{2\mu_{\rm FZ}\left(\beta_{\rm FZ}^{-2} - c^{-2}\right)^{1/2}\mu_{\rm HS}\left(c^{-2} - \beta_{\rm HS}^{-2}\right)^{1/2}}{\mu_{\rm FZ}^2\left(\beta_{\rm FZ}^{-2} - c^{-2}\right) - \mu_{\rm HS}^2\left(c^{-2} - \beta_{\rm HS}^{-2}\right)}, \quad (2)$$

where W is the FZ width, c is the phase velocity, f is the frequency, and $\mu_{\rm HS}$ and $\mu_{\rm FZ}$ are shear moduli of the HS and FZ layer, respectively. The results show that our procedure for measuring group velocities provides values that match the analytic group velocity solution well.

Ben-Zion (1998) illustrated various trade-offs between model parameters with time-domain calculations. The following two examples illustrate similar trade-offs in the frequency domain. Fig. 11(a) shows comparisons of analytical and numerical dispersion curves for different FZ parameters. The measured group velocities for synthetic seismograms with $Q_{\rm FZ} = 1000$ match the analytic group velocity solution well over most of the frequency range, and underestimate somewhat the analytic results at low frequencies. As Q decreases, the measured dispersion curves shift downwards and at $Q_{\rm FZ} = 10$ the measured group velocities deviate over the entire frequency range from the analytic dispersion curves by approximately 0.2 km s^{-1}. The effect of Q on the dispersion curves can also be produced by adjusting other FZ parameters. For example, if we increase the FZ width from 200 to 350 m, or decrease the HS and FZ shear velocities from 3 and 2 to 2.8 and 1.8 km s^{-1}, respectively, the analytic dispersion curves become close to the measured group velocities over most of the frequency ranges with the previous set of parameters and $Q_{\rm FZ} = 10$.

In Fig. 11(b), the lines are generated by the analytical dispersion formula using $\beta_{\rm HS} = 3$ km s^{-1}, $\beta_{\rm FZ} = 2$ km s^{-1}, $Q_{\rm FZ} = 50$ and $W = 200$ m. The different symbols represent group velocities measured from the synthetic seismograms with different propagation distances, ranging from 1 to 15 km, along the FZ. The measured dispersion is weak for propagation distances smaller than 4 km and improves with increasing distances. As illustrated in Fig. 11(a), the downward shift of the measured dispersion curves at short propagation distance can also be produced by adjusting other FZ parameters properly.

Fig. 12(a) illustrates a dispersion analysis on the observed fault-parallel seismogram recorded at station E02 for event 10161206. The seismogram is first windowed 1 s before and 4 s after the S arrival. After applying a cosine taper with 5 per cent of the entire width to both ends, we filter the waveform into 16 frequency bands ranging from 1.5 to 6 Hz with a 0.3 Hz interval. Fig. 12(b) shows the averaged dispersion curves measured from observed seismograms generated by eight events, four (10151352, 10150912, 10150914 and 10160717) north and four (10140848, 10150605, 10151139 and 10161206) south of the array. These eight events were selected

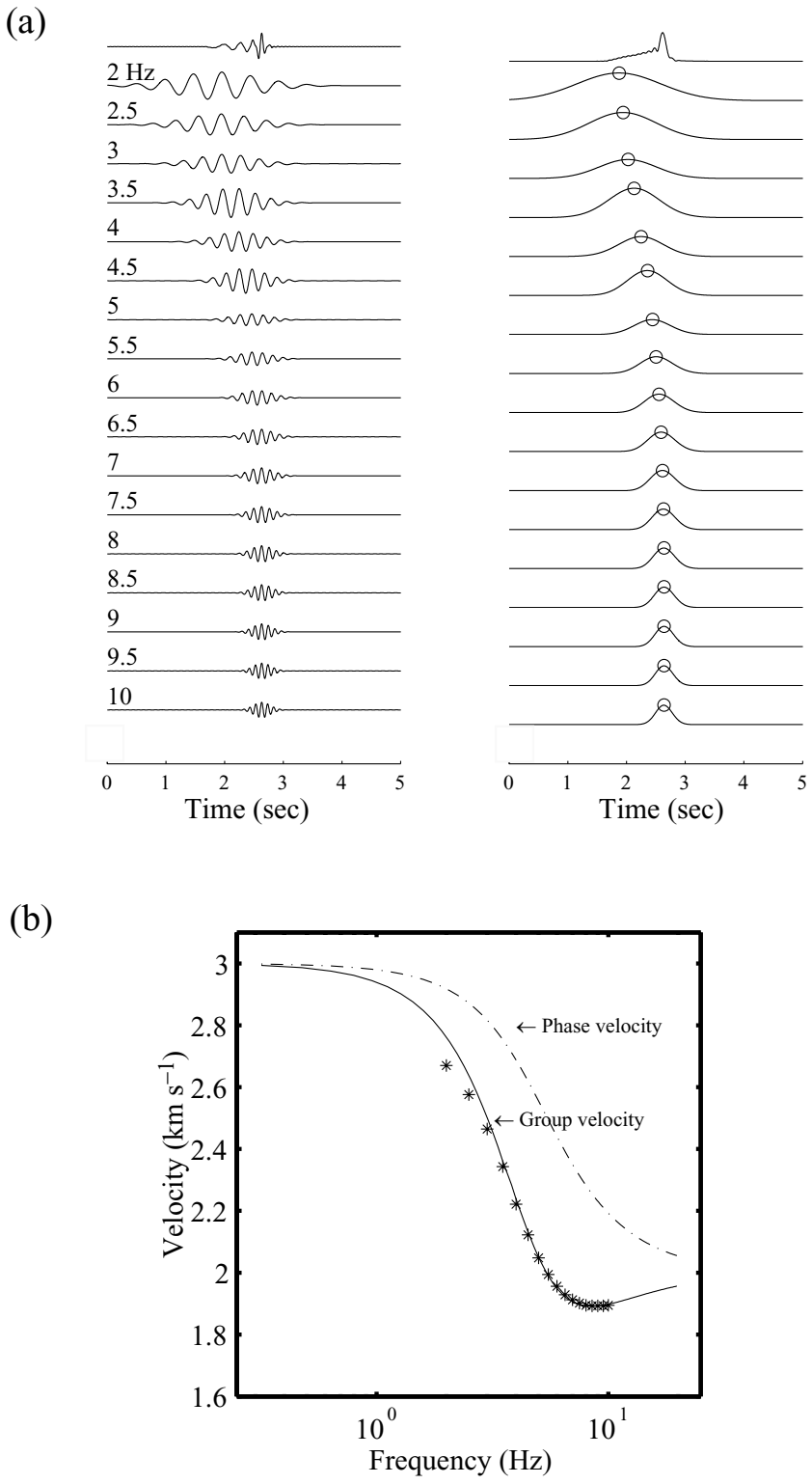

Figure 10. (a) Synthetic FZ seismograms (left) filtered at different frequency bands using a zero-phase Gaussian filter and envelopes of filtered seismograms calculated using the Hilbert transform (right). The peaks of the envelopes (circles) indicate the arrivals of the energy at different frequency bands. (b) Comparison of analytical and numerical dispersion curves. Stars are group velocities measured from filtered synthetic seismograms. Lines are generated by the analytical dispersion formula of Ben-Zion & Aki (1990).

based on their high signal-to-noise ratio waveforms and high quality values (above 5.5) of FZ trapped waves generation. The dispersion curves measured for events located north of the array are flatter than those located south of the array, suggesting that the velocity contrast, depth extent and other properties of the waveguide vary along the FZ. The dispersion measured from the observed data is in general rather weak, indicating short propagation distances inside the low-velocity FZ material. The results again imply that the trapping

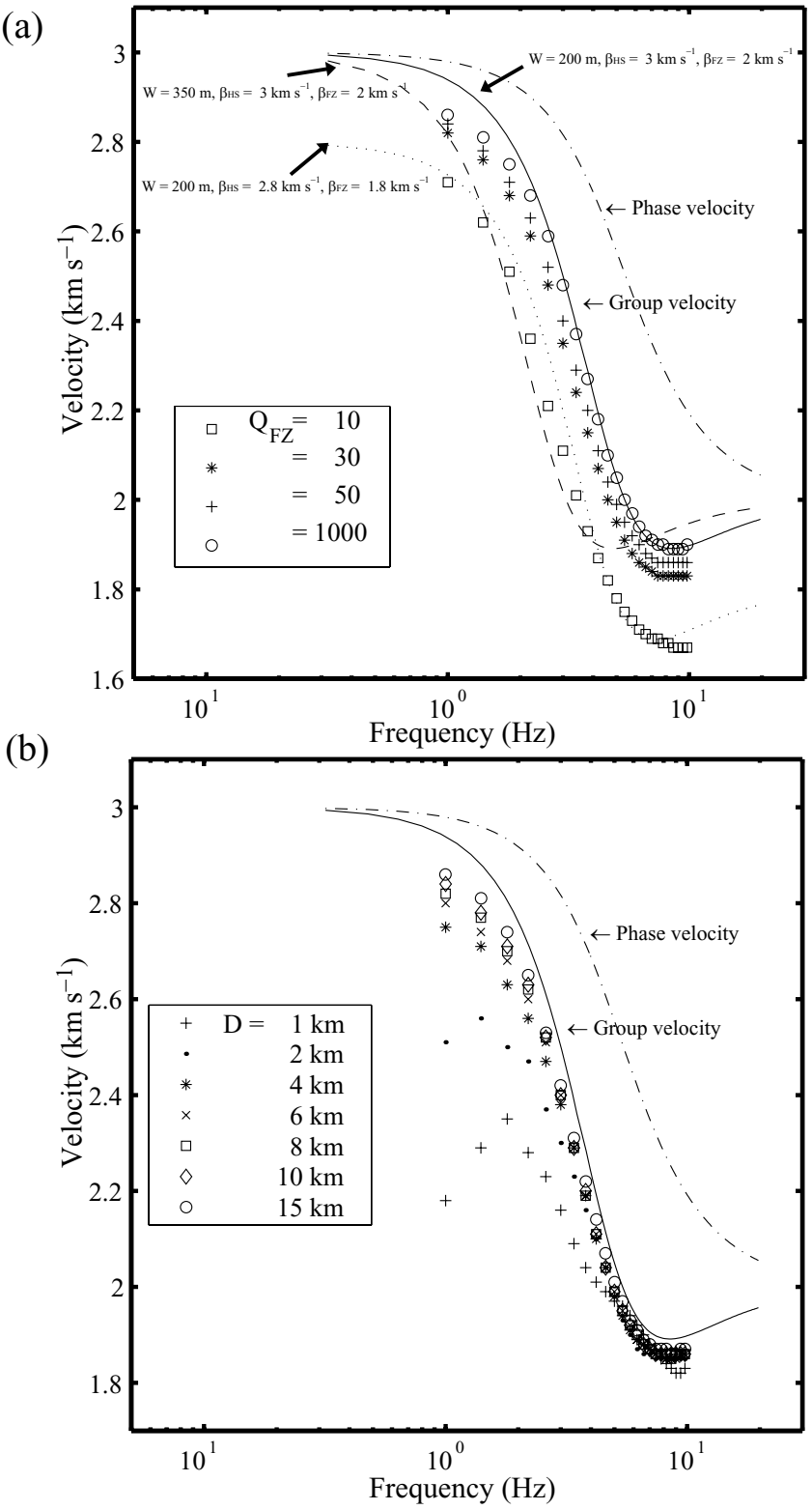

Figure 11. (a) Comparison of analytical and numerical dispersion curves for different FZ parameters. The points are group velocities measured from synthetic seismograms generated with different Q values. Other FZ parameters are the same as those used to produce the synthetic seismograms of Fig. 10(a). The lines are calculated using the analytical dispersion formula for various model parameters as indicated in the figure. The results illustrate trade-offs between FZ parameters in the frequency domain. (b) Comparison of analytical and numerical dispersion curves for different propagation distances along the FZ. The symbols mark group velocities measured from the synthetic seismograms of Fig. 7(a) with different propagation distances. Lines are generated by the analytical dispersion formula of Ben-Zion & Aki (1990). The dispersion is poor for distances smaller than approximately 4 km and improves with increasing propagation distance.

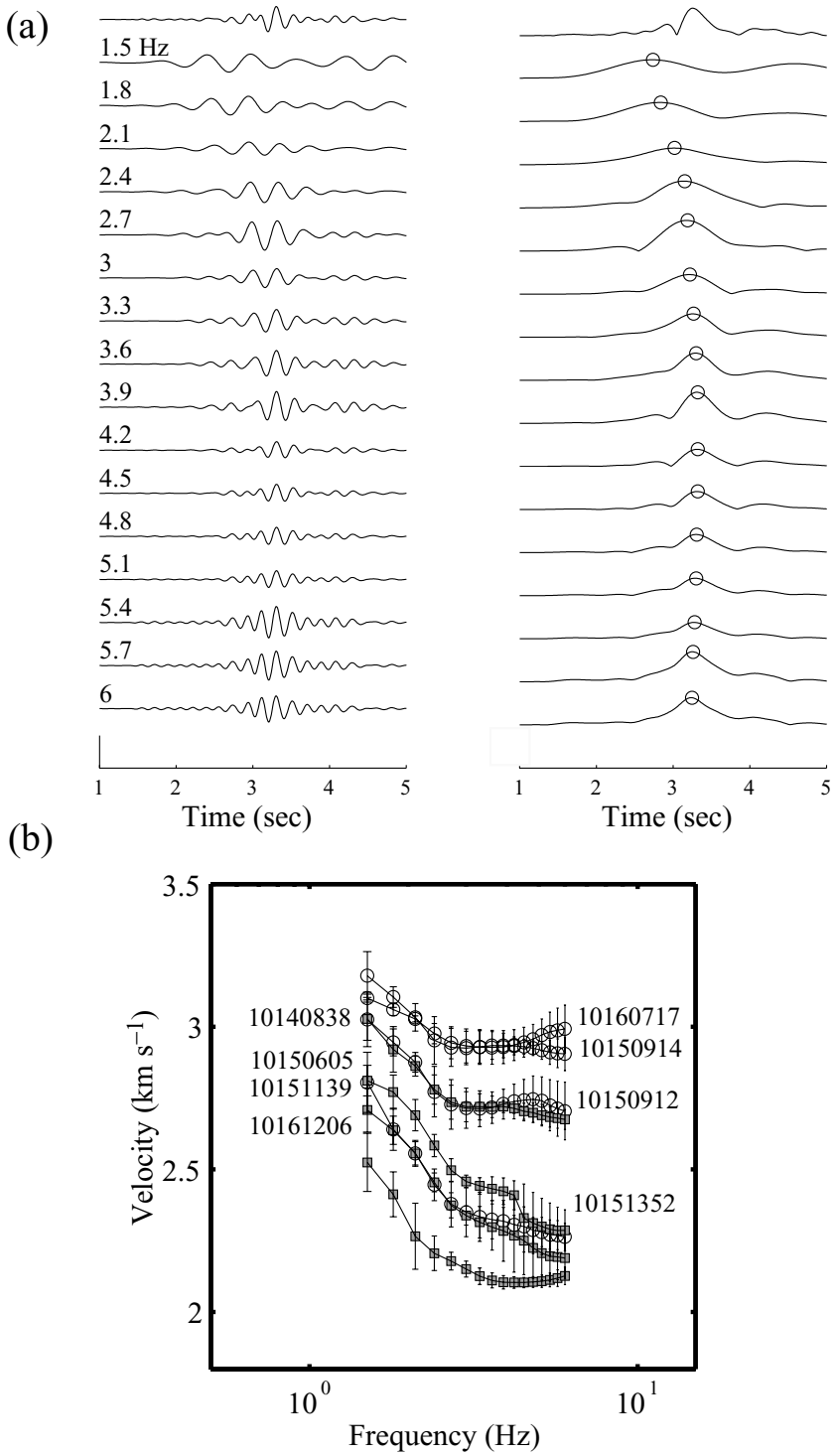

Figure 12. (a) Different frequency bands of a fault-parallel seismogram recorded at station E02 for event 10161206 (left) and envelopes of the bandpass-filtered waveforms (right). (b) Average dispersion curves measured from seismograms recorded at FZ stations W01–E05 for eight events with ID numbers marked in the figure. The locations of the events are marked in Fig. 3(a). Squares and circles denote the values for events south and north of the array, respectively. Each point gives the average group velocities in the specified frequency band measured from seismograms recorded at the six stations (W01–E05) that are close to the fault trace. The error bar at each point is the standard deviation of the result. Waveforms of these events are modelled in Figs 13 and 14.

of seismic energy in the Landers rupture zone is generated by a shallow FZ layer. The trade-offs among FZ parameters illustrated in Fig. 11 imply that results based on dispersion of FZ trapped waves do not provide strong constraints on the parameters of the velocity structure.

2.5 Synthetic waveform modelling of FZ trapped waves

In this section we model portions of observed FZ seismograms with trapped waves using the 2-D analytical solution of Ben-Zion & Aki (1990) and Ben-Zion (1998) for a plane-parallel layered FZ

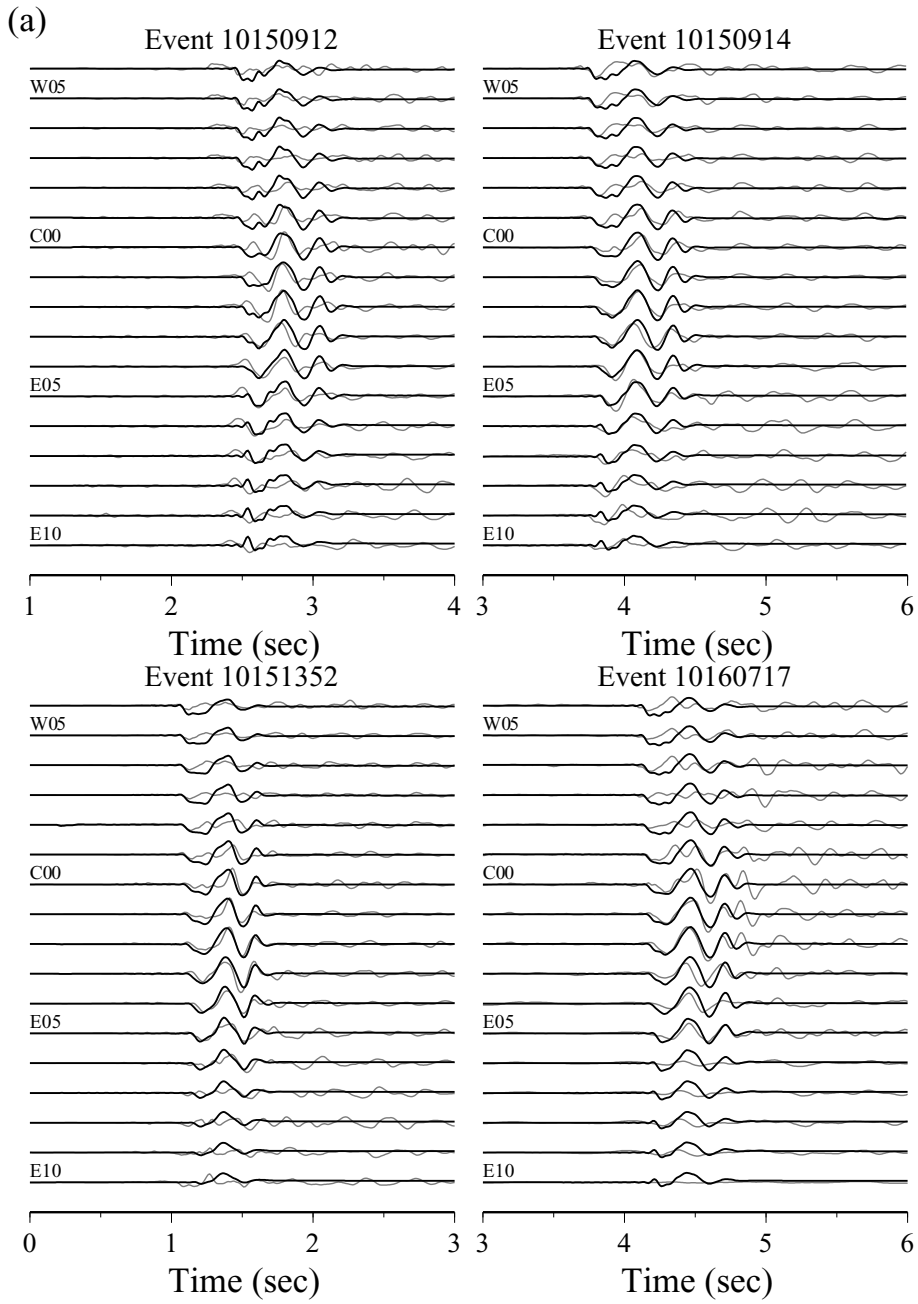

Figure 13. (a) Simultaneous synthetic (dark lines) waveform fits of 68 fault-parallel displacement seismograms (light lines) recorded by the 17 stations across the FZ and generated by four events north of the array. The locations of the events are marked in Fig. 3(a). (b) Fitness values (dots) associated with different FZ parameters tested by the GIA. The model parameters associated with the highest fitness values (solid circles) were used to generate the synthetic waveforms in (a). The curves give probability density functions for the various model parameters.

structure (Fig. 8). The model parameters include: (1) seismic velocities, attenuation coefficients and the width of the FZ layer; (2) seismic properties of the bounding blocks; and (3) source and receiver positions with respect to the fault and the free surface. As discussed by Ben-Zion *et al.* (2003), the 2-D analytical solution provides a proper modelling tool for trapped waves in FZ sections with width much smaller than the length and depth dimensions, and much larger than correlation lengths of internal material and geometrical heterogeneities. Igel *et al.* (1997) and Jahnke *et al.* (2002) showed with 3-D numerical calculations of wave propagation in irregular FZ structures that trapped waves are not sensitive to plausible velocity gradients with depth, gradual FZ boundaries, small-scale scatters and other types of smooth or small heterogeneities. In general, FZ trapped waves average out small internal 3-D variations and provide information on effective uniform waveguide properties over the observed range of wavelengths. Since trapped waves give the resonance response of the FZ structure after the transient source effects, the response to a line dislocation source can be converted accurately to an equivalent response to a point source by deconvolving the synthetic seismograms with $1/\sqrt{t}$ (e.g. Vidale *et al.* 1985; Crase *et al.* 1990; Igel *et al.* 2002; Ben-Zion *et al.* 2003). As illustrated in Figs 13 and 14, the 2-D analytical

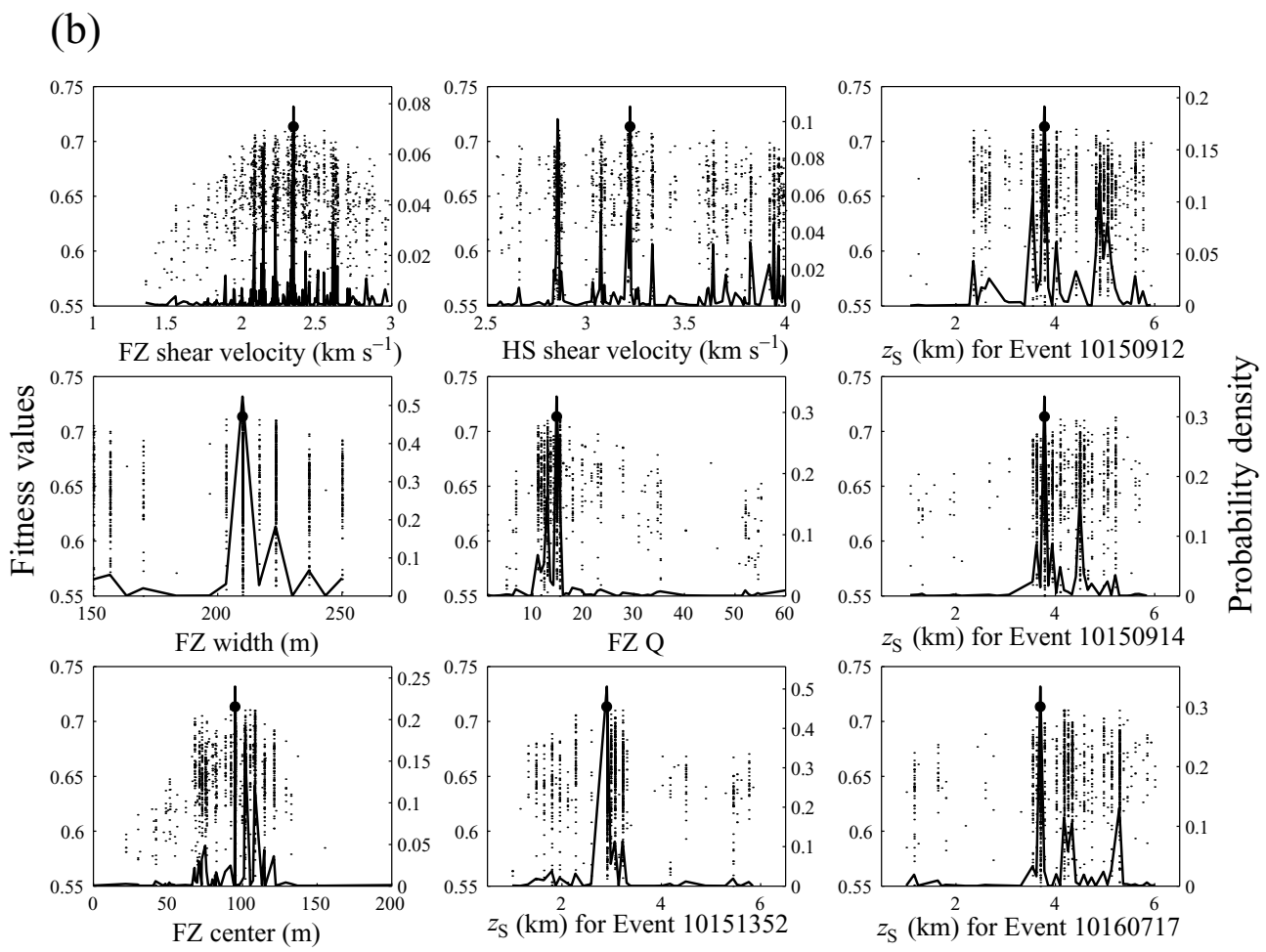

Figure 13. (*Continued.*)

solution provides very good waveform fits to the observed FZ trapped waves.

Ben-Zion (1998) emphasized that there are significant non-orthogonal trade-offs between the effective 2-D FZ parameters. The number N of internal reflections in the low-velocity layer controls the overall properties of the resulting interference patterns and trapped waves. This number depends on the FZ width, source–receiver distance and velocity contrast as

$$N = \frac{z_S}{W \tan(\theta_c)}, \tag{3}$$

where z_S is the propagation distance in the FZ layer and $\theta_c = \sin^{-1}(\beta_{FZ}/\beta_{HS})$ is the critical reflection angle at the interface between the FZ layer and HS. Other FZ parameters, such as source and receiver positions and attenuation coefficients of the FZ and HS media, also play important roles in modifying observed features of the resulting trapped waves. To model the data with a method that accounts quantitatively for the trade-offs, we use a genetic inversion algorithm (GIA) that employs the 2-D analytical solution as a forward kernel (Michael & Ben-Zion 1998). The inversion maximizes the correlations between observed and synthetic waveforms while performing a systematic and objective search of the relevant parameter space. In this study and our related works in the Parkfield section of the San Andreas fault (Michael & Ben-Zion 1998) and Karadere–Duzce branch of the North Anatolian fault (Ben-Zion *et al.* 2003), a single uniform FZ layer in an HS (Fig. 8) is sufficient to produce very good waveform fits to the observed data (see also Haberland *et al.* 2003).

Fig. 13(a) shows synthetic waveform fits (dark lines) of 68 fault-parallel displacement seismograms (grey lines) recorded by the 17 stations across the Landers rupture zone for events 10150912, 10151352, 10150914 and 10160717 north of the array. Prior to inversion, we remove from the data the mean and instrument response and convolve the seismograms with $1/\sqrt{t}$ to obtain equivalent 2-D line-source seismograms. The GIA calculates fitness values associated with different sets of model parameters. The fitness is defined as $(1 + C)/2$, where C is the cross-correlation coefficient between the observed and synthetic waveforms. The synthetic waveform fits of Fig. 13(a) were generated using the best-fitting parameters associated with the highest fitness value during 10 000 inversion iterations. We note that the waveform fits at stations relatively off the FZ are less satisfactory than at stations near the FZ, and that the onsets of the synthetic S body waves do not always fit the observed onsets well. These discrepancies are associated with the fact that the inversion method gives higher weight to phases with larger amplitudes, i.e. the trapped waves at the stations near the FZ.

Fig. 13(b) shows fitness values (dots) calculated by the GIA for the final 2000 iterations. The best-fitting values (solid circles) are

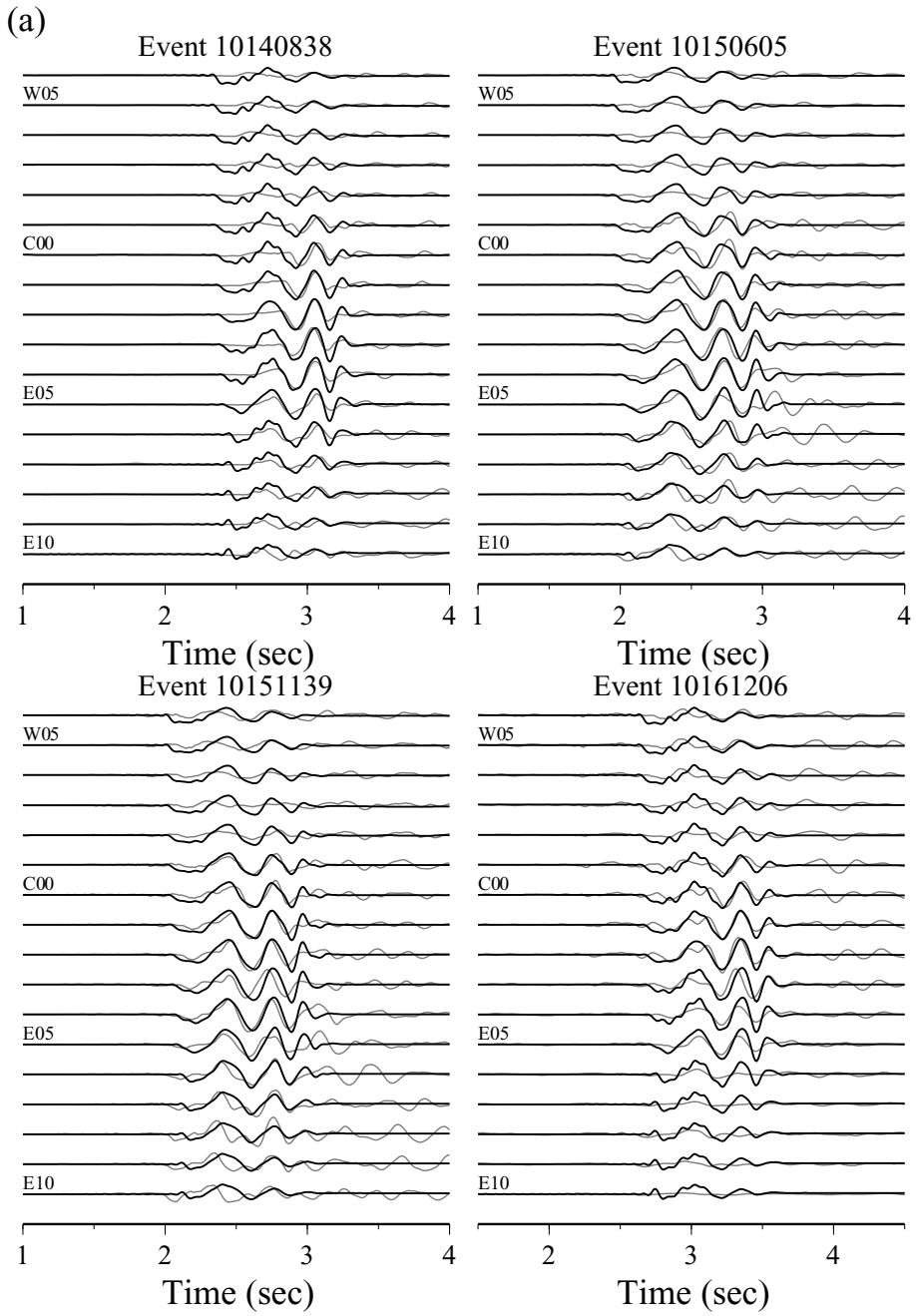

Figure 14. (a) Simultaneous synthetic (dark lines) waveform fits of displacement seismograms (light lines) recorded by the 17 stations across the FZ and generated by four events south of the array. (b) Fitness values (dots) associated with different FZ parameters tested by the GIA. The model parameters associated with the highest fitness values (solid circles) were used to generate the synthetic waveforms in (a). The curves show probability densities for the various model parameters.

$\beta_{FZ} = 2.3$, $\beta_{HS} = 3.2$ km s^{-1}, $W = 210$ m, $Q_{FZ} = 15$ and $z_S =$ 2.9, 3.8, 3.8 and 3.7 km. We obtain very good simultaneous fits to waveforms generated by four events with different locations using very similar propagation distances (of approximately 3–4 km) along the FZ. This again suggests that the trapping structure is shallow and does not extend continuously from the array location along strike over a distance larger than a few kilometres. The lines in Fig. 13(b) give probability density functions (PDFs) for the various model parameters, calculated by summing the fitness values and normalizing the results to have unit sums (Ben-Zion *et al.* 2003). The peaks in the PDFs provide another possible set of preferred model parameters. The peak probability values of the propagation distances in the FZ layer are also similar to each other and in the range of approximately 3–4 km. The modelling indicates further that the waveguide below the array is not centred at the exposed fault trace (station C00), but at a distance of approximately 100 m east

(b)

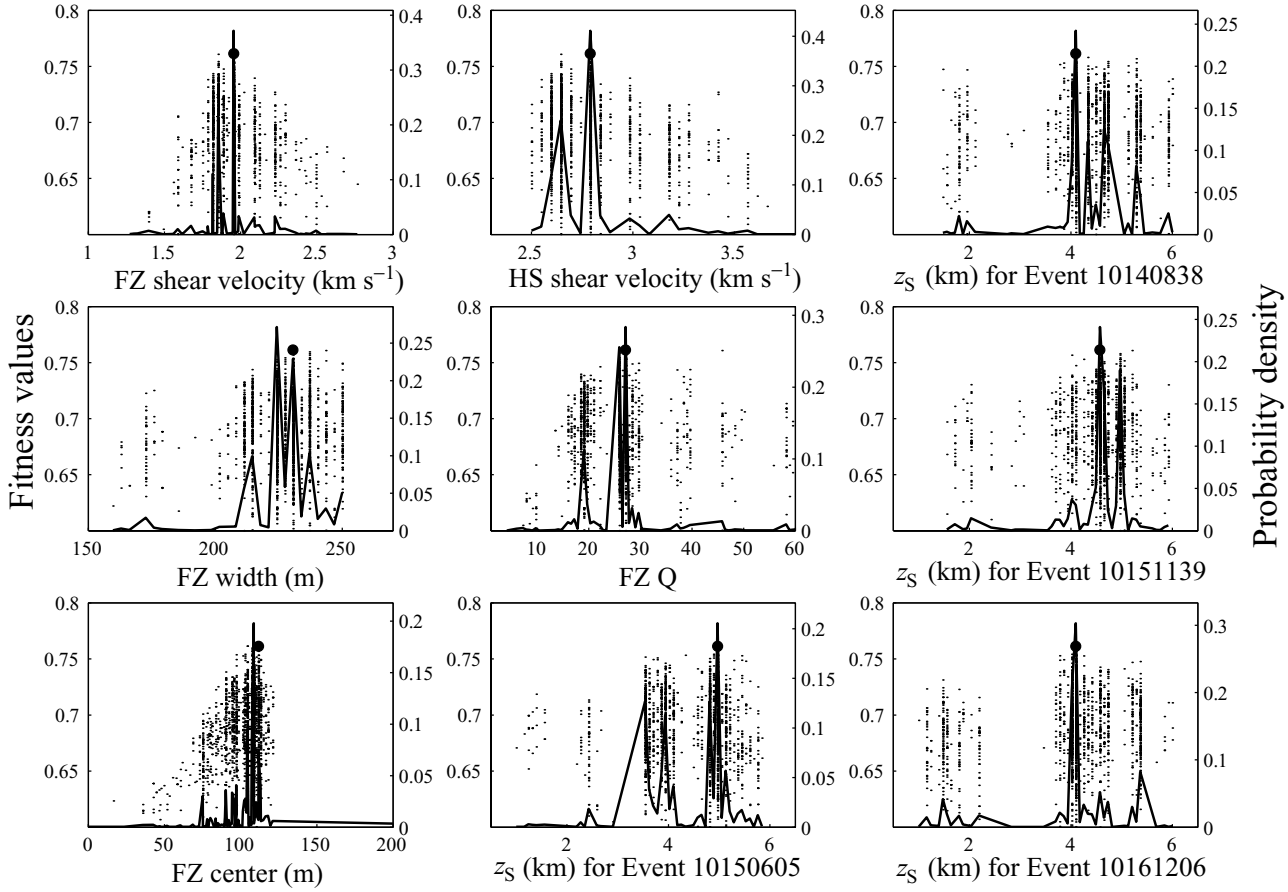

Figure 14. (*Continued.*)

of station C00. This is compatible with contour maps of normalized amplitude spectra distribution versus station positions of the types shown in Figs 4 and 5.

Fig. 14(a) shows synthetic waveform fits of the GIA to 68 fault-parallel displacement seismograms generated by events 10140838, 10150605, 10151139 and 10161206 south of the array. The synthetic waveforms were produced using the best-fitting parameters given in Fig. 14(b). The best-fitting values are $\beta_{FZ} = 2.0$, $\beta_{HS} = 2.8$ km s^{-1}, $W = 230$ m, $Q_{FZ} = 27$ and $z_S = 4.1$, 4.9, 4.6 and 4.1 km. As before, we obtain very good simultaneous fits to waveforms generated by earthquakes with different locations using similar propagation distances (of approximately 4–5 km) within the waveguide.

Since the eight events used in the synthetic waveform fits of Figs 13 and 14 are not located directly underneath the array, the propagation paths of the FZ trapped waves include along-strike components. Assuming (as was done in Section 2.4) that the average along-strike and vertical components are similar, we obtain estimated waveguide depth below the surface rupture of the Landers earthquake of approximately 2–3 km north of the array and 3–4 km south of it. We also note that the best-fitting values for the waveguide north and south of the array are different. These results, together with the relatively flat dispersion curves as shown in Fig. 12(b), suggest that the waveguide north of the array is somewhat shallower and weaker than that south of the array.

As discussed in the context of our work on the North Anatolian fault (Ben-Zion *et al.* 2003), we can obtain very good fits between synthetic and observed waveforms for a wide range of parameters due to the strong trade-offs between parameters (Ben-Zion 1998). It is thus important to use independent constraints on parameter values if such are available. The inversions leading to the results of Figs 13 and 14 were done assuming that the FZ width is in the range 150–250 m, in agreement with field observations (Johnson *et al.* 1994, 1997; Li *et al.* 1994a,b; Rockwell *et al.* 2000) on the width of the surface rupture zone of the Landers earthquake in our study area. We can produce good waveform fits for larger propagation distance inside the waveguide than those of Figs 13 and 14, but this tends to increase the FZ width beyond the observed ≈200 m *in situ* value.

3 DISCUSSION

We perform a comprehensive analysis of a waveform data set generated by 238 aftershocks and recorded by a dense seismic array across and along the rupture zone of the 1992 Landers earthquake. Events recorded only by the dense array are located by a grid search and station corrections method (Figs 2 and 3a). Based on the ratio of trapped waves to *S*-wave energy, we assign a quality A, B or C of trapped waves generation to 198 events (inset of Fig. 3a).

Approximately 70 per cent of nearby events with *S–P* time of less than 2 s, including many clearly off the fault, generate FZ trapped waves of quality A or B (Fig. 3). This spatial distribution differs from previous claims (e.g. Li *et al.* 1994a,b, 2000) that trapped waves at the Landers rupture zone are generated only by sources very close to or inside the FZ. Igel *et al.* (2002), Jahnke *et al.* (2002) and Fohrmann *et al.* (2003) demonstrated that a shallow FZ layer can trap seismic energy generated by events that are deeper and well outside it, while generation of trapped waves in a deep and coherent FZ layer requires the source to be close or inside the FZ. The existence of trapped waves due to sources outside the rupture zone of the Landers earthquake implies that the generating structure is shallow. This statement is further supported by traveltime data of *S* and trapped waves (Fig. 9), dispersion analysis (Fig. 12) and synthetic waveform modelling (Figs 13 and 14).

We could model all the waveforms generated by the 34 events that produce trapped waves with quality A. However, this will not significantly increase the imaging resolution because of the relatively short propagation distances inside the FZ waveguide and the trade-offs between model parameters that are reflected in the parameter space plots (Figs 13b and 14b). We thus provide quantitative waveform fits only for 136 waveforms generated by the eight events used in the dispersion analysis. Since clear trapped waves are not recorded at stations W11–W07, in the inversions we only use waveforms recorded by 17 (W06–E10) out of 22 stations of the east–west FZ array.

The synthetic waveform modelling indicates that the FZ waveguide has a depth of approximately 2–4 km, a width of the order of 200 m, an *S*-wave velocity reduction relative to the host rock of approximately 30–40 per cent and an *S*-wave attenuation coefficient of approximately 20–30. The modelling also shows that the waveguide below the array is not centred at the exposed fault trace (station C00), but at a distance of approximately 100 m east of station C00. The waveform modelling and dispersion analysis suggest that the waveguide north of the array is possibly shallower and weaker than that south of the array. The traveltime analysis also suggests that the FZ waveguide in our study area is not continuous along strike for more than a few kilometres.

Shallow trapping structures with similar properties appear to characterize the Karadere–Duzce branch of the North Anatolian fault (Ben-Zion *et al.* 2003), the Parkfield segment of the San Andreas fault (Michael & Ben-Zion 1998; Korneev *et al.* 2003) and the Anza segment of the San Jacinto fault (Lewis *et al.* 2003). Shallow layers of damaged FZ rock acting as seismic waveguides can exist not only in active structures but also (Rovelli *et al.* 2002; Cultrera *et al.* 2003) in dormant fault zones. Ben-Zion *et al.* (2003) suggested that shallow trapping structures are a common element of fault zones and may correspond to the top part of a flower-type structure. Since the volume of sources capable of generating motion amplification in shallow FZ waveguides is large, the existence of such structures increases the seismic shaking hazard near faults (Spudich & Olsen 2001; Ben-Zion *et al.* 2003).

Our results indicate that approximately 70 per cent of the events with an *S–P* time of less than 2 s are able to generate trapped wave energy at the Landers rupture zone exceeding the *S*-wave energy by a factor of 2 or more (quality A or B). The source volume percentage is comparable to that estimated by Fohrmann *et al.* (2003) using 3-D finite-difference calculations, but smaller than that observed by Ben-Zion *et al.* (2003) along the Karadere–Duzce branch of the North Anatolian fault. Possible explanations for the more abundant generation of trapped waves in the Karadere–Duzce fault may be the greater diversity of focal mechanisms and the greater depth of hypocentres. As pointed out by Fohrmann *et al.* (2003), the volume of sources capable of generating trapped waves at shallow structures increases with depth, and the amount of generated energy depends on the receiver position within the radiation pattern of the events. Thus, the overall potential of generating trapped waves energy increases with the depth of seismicity and diversity of focal mechanisms. Seeber *et al.* (2000) and Ben-Zion *et al.* (2003) found that most hypocentres around the Karadere–Duzce branch of the 1999 Izmit earthquake rupture are deeper than 5 km, and noted that the focal mechanisms of the events are likely to be highly diverse. In contrast, approximately 50 per cent of the 93 events with catalogue locations in our data set have hypocentres shallower than 5 km and the events are likely to be dominated by strike-slip focal mechanisms.

We note that the overall pattern of our event locations (Figs 2a and 3a) is similar to the pattern of the catalogue locations, although there are differences in the locations of individual events. We have tried several other location techniques, such as plane-wave fitting and the double-difference algorithm (Waldhauser 2001) with waveform cross-correlation, but were not able to significantly improve the locations. Our location procedure employs a 1-D velocity model because a 3-D model with the fault zone structure in our study area is not available. However, the quality of earthquake locations obtained with 1-D velocity model and station corrections is generally comparable to that produced by a 3-D model (e.g. Eberhart-Phillips & Michael 1998). The real limitation for obtaining better locations using only the phase picks recorded at the FZ array stems from the fact that the array aperture is only approximately 1 km. Unfortunately, most events that generate FZ trapped waves with quality A or B in our data set are not recorded by the SCSN and hence do not have catalogue locations. We suggest that in future designs of similar experiments, a number of stations should be installed off the fault, as was done in our related study on the Karadere–Duzce fault (Seeber *et al.* 2000; Ben-Zion *et al.* 2003), to have sufficient regional coverage for accurate determination of event locations.

ACKNOWLEDGMENTS

We thank Willie Lee for providing us with the waveform data set used in this work. The manuscript benefited from useful comments by Michael Korn, Deborah Kilb and an anonymous reviewer. The study was supported by the Southern California Earthquake Center (based on NSF cooperative agreement EAR-8920136 and USGS cooperative agreement 14-08-0001-A0899).

REFERENCES

Aki, K. & Richards, P.G., 2002. *Quantitative Seismology,* 2nd edn, University Science Books, Sausalito, CA.

Ben-Zion, Y., 1998. Properties of seismic fault zone waves and their utility for imaging low velocity structures, *J. geophys. Res.,* **103,** 12 567–12 585.

Ben-Zion, Y. & Aki, K., 1990. Seismic radiation from an SH line source in a laterally heterogeneous planar fault zone, *Bull. seism. Soc. Am.,* **80,** 971–994.

Ben-Zion, Y. & Sammis, C.G., 2003. Characterization of fault zones, *Pure appl. Geophys.,* **160,** 677–715.

Ben-Zion, Y. *et al.*, 2003. A shallow fault zone structure illuminated by trapped waves in the Karadere–Duzce branch of the North Anatolian Fault, western Turkey, *Geophys. J. Int.,* **152,** 699–717.

Crase, E., Pica, A., Noble, M., McDonald, J. & Tarantola, A., 1990. Robust elastic nonlinear inversion: application to real data, *Geophysics,* **55,** 527–538.

Chester, F.M. & Chester, J.S., 1998. Ultracataclasite structure and friction processes of the Punchbowl fault, San Andreas system, California, *Tectonophysics,* **295,** 199–221.

Cultrera, G., Rovelli, A., Mele, G., Azzara, R., Caserta, A. & Marra, F., 2003. Azimuth-dependent amplification of weak and strong ground motions within a fault zone (Nocera Umbra, central Italy), *J. geophys. Res.,* **108,** 2156, doi:10.1029/2002JB001 929.

Eberhart-Phillips, D. & Michael, A.J., 1998. Seismotectonics of the Loma Prieta, California, region determined from three-dimensional V_p, V_p/V_s, and seismicity, *J. geophys. Res.,* **103,** 21 099–21 120.

Evans, J.P., Shipton, Z.K., Pachell, M.A., Lim, S.J. & Robeson, K., 2000. The structure and composition of exhumed faults, and their implication for seismic processes, in *Proc. 3rd Conf. on Tectonic Problems of the San Andreas System,* Stanford University.

Faulkner, D.R., Lewis, A.C. & Rutter, E.H., 2003. On the internal structure and mechanics of large strike-slip fault zones: field observations of the Carboneras fault in southeastern Spain, *Tectonophysics,* **367,** 235–251.

Fialko, Y., Sandwell, D., Agnew, D., Simons, M., Shearer, P. & Minster, B., 2002. Deformation on nearby faults induced by the 1999 Hector Mine earthquake, *Science,* **297,** 1858–1862.

Fohrmann, M., Jahnke, G., Igel, H. & Ben-Zion, Y., 2003. Guided waves from sources outside faults: an indication for shallow fault zone structure?, *Pure appl. Geophys.,* in press.

Haberland, C., Agnon, N.A., El-Kelani, R., Maercklin, N., Qabbani, I., Rumpker, G., Ryberg, T., Scherbaum, F. & Weber, M., 2003. Modeling of seismic guided waves at the Dead Sea Transform, *J. geophys. Res.,* **108**(B7), 2342.

Hauksson, E., Jones, L.M., Hutton, K. & Eberhart-Phillips, D., 1993. The Landers earthquake sequence: Seismological observations, *J. geophys. Res.,* **98,** 19 835–19 853.

Igel, H., Ben-Zion, Y. & Leary, P., 1997. Simulation of SH and *P–SV* wave propagation in fault zones, *Geophys. J. Int.,* **128,** 533–546.

Igel, H., Jahnke, G. & Ben-Zion, Y., 2002. Numerical simulation of fault zone guided waves: accuracy and 3-D effects, *Pure appl. Geophys.,* **159,** 2067–2083.

Jahnke, G., Igel, H. & Ben-Zion, Y., 2002. Three-dimensional calculations of fault zone guided wave in various irregular structures, *Geophys. J. Int.,* **151,** 416–426.

Johnson, A.M., Fleming, R.W. & Cruikshank, K.M., 1994. Shear zones formed along long, straight traces of fault zones during the 28 June 1992 Landers, California, earthquake, *Bull. seism. Soc. Am.,* **84,** 499–510.

Johnson, A.M., Fleming, R.W., Cruikshank, K.M., Martosudarmo, S.Y., Johnson, N.A. & Johnson, K.M., 1997. Analecta of structures formed during the 28 June 1992 Landers-Big Bear, California earthquake sequence, Technical report, *US Geol. Surv. Open File Rep.,* 97–94.

Korneev, V.A., Nadeau, R.M. & McEvilly, T.V., 2003. Seismological studies at Parkfield IX: Fault-zone imaging using guided wave attenuation, *Bull. seism. Soc. Am.,* **93,** 1415–1426.

Lee, W.H.K., 1999. Digital waveform data of 238 selected Landers aftershocks from a dense PC-based seismic array, unpublished report, *US Geol. Surv.,* Menlo Park, CA.

Lewis, M.A, Peng, Z., Ben-Zion, Y. & Vernon, F.L., 2003. Shallow seismic trapping structure in the San Jacinto fault zone near Anza, California, *Seism. Res. Lett.,* **74,** 247.

Li, Y.G. & Leary, P., 1990. Fault zone seismic trapped waves, *Bull. seism. Soc. Am.,* **80,** 1245–1271.

Li, Y.G. & Vernon, F.L., 2001. Characterization of the San Jacinto fault zone near Anza, California, by fault zone trapped waves, *J. geophys. Res.,* **106,** 30 671–30 688.

Li, Y.G., Aki, K., Adams, D., Hasemi, A. & Lee, W.H.K., 1994a. Seismic guided waves trapped in the fault zone of the Landers, California, earthquake of 1992, *J. geophys. Res.,* **99,** 11 705–11 722.

Li, Y.G., Vidale, J.E., Aki, K., Marone, C.J. & Lee, W.H.K., 1994b. Fine-structure of the Landers fault zone—segmentation and the rupture process, *Science,* **265,** 367–370.

Li, Y.G., Aki, K., Vidale, J.E. & Alvarez, M.G., 1998. A delineation of the Nojima fault ruptured in the M7.2 Kobe, Japan, earthquake of 1995 using fault-zone trapped waves, *J. geophys. Res.,* **103,** 7247–7263.

Li, Y.G., Vidale, J.E., Aki, K. & Xu, F., 2000. Depth-dependent structure of the Landers fault zone using fault zone trapped waves generated by aftershocks, *J. geophys. Res.,* **105,** 6237–6254.

Li, Y.G., Vidale, J.E., Day, S.M., Oglesby, D.D. & the SCEC Field Working Team, 2002. Study of the 1999 M 7.1 Hector Mine, California, earthquake fault plane by trapped waves, *Bull. seism. Soc. Am.,* **92,** 1318–1332.

Michael, A.J. & Ben-Zion, Y., 1998. Challenges in inverting fault zone trapped waves to determine structural properties, *EOS, Trans. Am. geophys. Un.,* **79,** S231.

Mooney, W.D. & Ginzburg, A., 1986. Seismic measurements of the internal properties of fault zones, *Pure appl. Geophys.,* **124,** 141–157.

Richards-Dinger, K.B. & Shearer, P.M., 2000. Earthquake locations in southern California obtained using source specific station terms, *J. geophys. Res.,* **105,** 10 939–10 960.

Rockwell, T.K., Lindvall, S., Herzberg, M., Murbach, D., Dawson, T. & Berger, G., 2000. Paleoseismology of the Johnson Valley, Kickapoo, and Homestead Valley faults: clustering of earthquakes in the eastern California shear zone, *Bull. seism. Soc. Am.,* **90,** 1200–1236.

Rovelli, A., Caserta, A., Marra, F. & Ruggiero, V., 2002. Can seismic waves be trapped inside an inactive fault zone? The case study of Nocera Umbra, central Italy, *Bull. seism. Soc. Am.,* **92,** 2217–2232.

Scholz, C.H., 2002. *The Mechanics of Earthquakes and Faulting,* Cambridge University Press, New York.

Seeber, L., Armbruster, J.G., Ozer, N., Aktar, M., Baris, S., Okaya, D., Ben-Zion, Y. & Field, E., 2000. The 1999 Earthquake Sequence along the North Anatolia Transform at the juncture between the two main ruptures, in *The 1999 Izmit and Duzce Earthquakes: Preliminary Results,* pp. 209–223, ed. Barka *et al.*, Istanbul Technical University, Istanbul.

Sibson, R.H., 2002. Geology of the crustal earthquake source, in *International Handbook of Earthquake and Engineering Seismology, Part A,* eds Lee, W.H.K., Kanamori, H., Jennings, P.C. & Kisslinger, C., pp. 455–473, Academic Press, San Diego.

Sieh, K. *et al.*, 1993. Near-field investigations of the Landers earthquake sequence, April to July 1992, *Science,* **260,** 171–176.

Spudich, P. & Olsen, K.B., 2001. Fault zone amplified waves as a possible seismic hazard along the Calaveras fault in central California, *Geophys. Res. Lett.,* **28,** 2533–2536.

Waldhauser, F., 2001. HypoDD-A program to compute double-difference hypocenter location, *US Geol. Surv. Open File Rep.,* 01–113.

Vidale, J.E., Helmberger, D.V. & Clayton, R.W., 1985. Finite-difference seismograms for SH waves, *Bull. seism. Soc. Am.,* **75,** 1765–1782.